A class of energy stable, high-order finite-difference interface schemes suitable for adaptive mesh refinement of hyperbolic problems

R.M.J. Kramer *, C. Pantano, D.I. Pullin

Graduate Aeronautical Laboratories, California Institute of Technology, MC 205-45, Pasadena, CA 91125, United States

Abstract

We present a class of energy stable, high-order finite-difference interface closures for grids with step resolution changes. These grids are commonly used in adaptive mesh refinement of hyperbolic problems. The interface closures are such that the global accuracy of the numerical method is that of the interior stencil. The summation-by-parts property is built into the stencil construction and implies asymptotic stability by the energy method while being non-dissipative. We present one-dimensional closures for fourth-order explicit and compact Padé type, finite differences. Tests on the scalar one- and two-dimensional wave equations, the one-dimensional Navier–Stokes solution of a shock and two-dimensional inviscid compressible vortex verify the accuracy and stability of this class of methods.
© 2007 Elsevier Inc. All rights reserved.

Keywords: High-order finite difference; Mesh-interface; Stable stencil; Adaptive mesh refinement

1. Introduction

As structured adaptive mesh refinement (AMR) becomes more popular, in fluid dynamics and other hyperbolic systems, there is a need for improved accuracy and stability of the numerical methods [1]. These issues play an important role when dealing with flow features that are sensitive to numerical dissipation, such as turbulence and general wave-propagation problems. A compelling feature of AMR is the improved computational performance achieved by the use of relatively simple data structures. This also enables dynamic adaptivity, since implementation details are not riddled by grids with a large number of topologically different mesh interfaces. For example, the method of [2,3] is among the most widely used and it consists essentially of a finite-volume type hierarchical partition of the domain and a logically Cartesian patch-based recursive algorithm. The mesh at different levels is properly nested to avoid an excessive number of mesh-interface types. In [3], the key simplification in the interface treatment lies in the communication of information from coarse to

---

fine meshes through an interpolation/restriction operation on the conservative vector of state. That is, the coarse vector of state is interpolated to guard fine cells adjacent to the mesh boundary and the vector of state is restricted (averaged) in the fine mesh to fill guard coarse cells. While this can be made computationally efficient, the simple interpolation operation is not easily extensible to high-order discretizations while at the same time preserving stability, without introducing artificial numerical dissipation [4–6].

In the development of methods used at mesh interfaces defined by step changes in resolution, the standard approach used to-date involves choosing the coefficients of the interface stencil by satisfying local stability criteria. This has been utilized in second-order finite-volume (FV) [7,8] and finite-difference (FD) [9] methods. The stability properties of the interface stencils are analyzed typically by an eigenvalue analysis, where the rigorous GKS theory [10] is generally a starting point [11,12]. Unfortunately, as shown by [13], stability must be analyzed carefully when the mesh includes more than one interface, since there is no guarantee that a single stable interface treatment will lead to multiple stable interfaces. The presence of multiple interfaces can lead to algebraic, and even in some cases exponential growth of perturbations even though each individual interface is locally stable. The only rigorous approach to develop stable multiple-interface treatments is the use of a global stability criteria. It is largely this reason that makes energy stable methods desirable, since their global stability domain can be proven in most cases analytically. The recent energy stable second-order method of Ref. [14] belongs to this category. Moreover, energy stable methods have some desirable numerical properties; they tend to self diagnose the appropriate resolution (or lack thereof) required by the physical problem at hand. When the resolution is not sufficient, they generate numerical reflections off the mesh-interface when features that are well supported on the fine grid side try to propagate over an under-resolved coarse grid. This and other properties of non-uniform meshes were identified early [15–17] and arise for most methods that are not overly dissipative. The problem of stability on a grid with continuously variable resolution is discussed in [16], and is not considered here.

The use of high-order methods with grid resolution jumps is less developed. On one hand, FD methods tend to be more convenient than finite-volume methods because there is no need to retrieve the interpolant from the nodal volume averaged values of the FV, nor is there a need for a high-order quadrature to construct the cell face fluxes. On the other hand, there is an advantage of using a FV mesh topology since there are no overlapping nodes and it is easy to refine/coarsen the solution vector for AMR. Furthermore, high-order FD boundary stencils that are energy stable [18–20] have been derived only recently. The stencils are such that the boundary discretization satisfies the summation-by-parts (SBP), the GKS stability criteria and the time or asymptotic stability criteria. High-order interface methods are less mature. Ref. [21] has proposed a high-order FD interface scheme that uses the stable boundary stencils with a specially adapted penalty technique. This method requires a common point on both sides of the mesh, essentially a vertex type mesh, and ensures continuity of the function value and the first derivative, and can be viewed as a one-point overlapping mesh. This penalty technique does contribute to some numerical dissipation but it does not seem to be as large as with other methods and it has been used successfully in electromagnetic problems [22]. Related work has also been done for the elliptic Poisson equation [23], where time stability is not an issue.

The purpose of this paper is to develop a FD interface closure for a structured AMR-type grid that is of high accuracy and, at the same time, energy stable (non-dissipative and asymptotically stable) for first-order hyperbolic problems.

2. Interface closure statement

The starting point for this work is the following Cauchy problem, where the solution of the scalar advection equation

$$\frac{\partial u}{\partial t} + \lambda \frac{\partial u}{\partial x} = 0, \quad 0 \leqslant x \leqslant L, \ t \geqslant 0, \tag{1}$$

with an initial condition

$$u(x,0) = f(x), \quad 0 \leqslant x \leqslant L, \tag{2}$$

and the boundary condition at $x = 0$, for $\lambda > 0$,

$$u(0,t) = g(t), \quad t \geqslant 0, \tag{3}$$

is sought numerically.

Consider a partitioning of the spatial domain into M blocks, and that within each block a uniform nodal discretization of the coordinate x into N_m nodes with spacing h_m is performed. Grid interfaces are identified with the notation $1:r_m$, representing the interface between blocks with discretization h_m and h_{m+1}, where r_m is the mth interface grid ratio h_{m+1}/h_m. This discretization yields a total of $N = \sum_{m=1}^{M} N_m$ nodes, at locations x_i, with $i = 1, \ldots, N$. Fig. 1 depicts such a grid for a case with a single interface and where the locations of the nodal values x_j, relative to the origin at the interface, are given by

$$x_j = \begin{cases} h(\frac{1}{2} + j), & j < 0, \\ rh(\frac{1}{2} + j), & j \geqslant 0. \end{cases} \tag{4}$$

Consider a semi-discretization of Eq. (1) in space using the finite-difference approximation to the first-order derivative of a function $u(x)$, evaluated at the nodal locations x_i,

$$P\frac{d\mathbf{u}}{dx} = \frac{1}{h} Q\mathbf{u}, \tag{5}$$

where $\mathbf{u}$ is a vector of length N whose elements are $u_i = u(x_i)$, and P and Q are $N \times N$ banded matrices. The matrix Q is generally a Toeplitz matrix except for small perturbations at the boundaries and interfaces. The elements of these matrices are determined by solving the order conditions, derived from the Taylor series expansion of the zth-degree polynomial function

$$f_z(x) \equiv x^z, \tag{6}$$

about the point x_i, in terms of its value at neighbouring points x_j. The parameter h in Eq. (5) denotes the minimum value of all given h_m. For an approximation of the derivative to order s, the elements p_{ij} and q_{ij} must satisfy Eq. (5) with $u = f_z(x)$ exactly, for $z = 0, \ldots, s$:

$$zh \sum_{j=i-k}^{i+k} p_{ij}(x_j - x_i)^{z-1} = \sum_{j=i-k}^{i+k} q_{ij}(x_j - x_i)^z, \tag{7}$$

where the stencil has a width of $s + 1$ points for the interior of the domain, where $k = s/2$. For a general five-point centered scheme, away from boundaries, Q is a penta-diagonal matrix, and the derivative approximation at the interior points i has the familiar form

$$a\frac{du_{i-1}}{dx} + b\frac{du_i}{dx} + a\frac{du_{i+1}}{dx} = \frac{1}{h}(\beta(u_{i+1} - u_{i-1}) + \alpha(u_{i+2} - u_{i-2})). \tag{8}$$

For an explicit scheme, P can be chosen as the identity matrix, and for fourth-order accuracy, $\alpha = -\frac{1}{12}$ and $\beta = \frac{2}{3}$. For the classical fourth-order tri-diagonal Padé scheme with $\alpha = 0$ and $b = 1$, the coefficients are $a = \frac{1}{4}$, and $\beta = \frac{3}{4}$ [24].
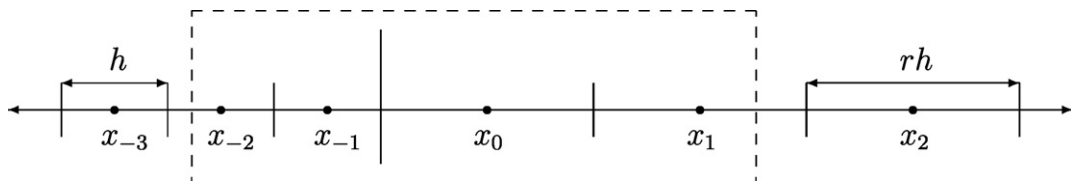

Fig. 1. Diagram showing an example of a grid interface: here, the four-point interface region lies inside the dashed box, with the interface lying between nodes x_{-1} and x_0. The node numbering scheme is local relative to the interface region.

3. Summation by parts and stability

According to the theory of [25,18,19], the following conditions must be satisfied for any discretization to be time or asymptotically stable and preserve the SBP property:

1. There exists a matrix H such that $V = HP$ is symmetric positive definite.
2. $W = HQ$ is an almost skew-symmetric matrix where the only non-zero terms on the diagonal are the first and last corner terms (for a finite-length domain), generally with $w_{11} < 0$ and $w_{NN} > 0$.
3. Stability requires that the structure of the matrix H at the boundary be that of a restricted or diagonal norm [18].

It is straightforward to show that under these conditions, the energy norm $E(t) = \lambda^{-1}(\mathbf{u}, HP\mathbf{u})$ of the semi-discrete version of Eq. (1) is conserved, and can be changed only by the boundary terms:

$$
\frac{dE}{dt} = \lambda^{-1}\left[\frac{d\mathbf{u}^{\mathrm{T}}}{dt}HP\mathbf{u} + \mathbf{u}^{\mathrm{T}}HP\frac{d\mathbf{u}}{dt}\right] = -\frac{1}{h}[(P^{-1}Q\mathbf{u})^{\mathrm{T}}HP\mathbf{u} + \mathbf{u}^{\mathrm{T}}(HQ\mathbf{u})] = -\frac{1}{h}[\mathbf{u}^{\mathrm{T}}[(HQ)^{\mathrm{T}} + HQ]\mathbf{u}]
$$

$$
= -\frac{1}{h}\left(w_{11}u_1^2 + w_{NN}u_N^2\right) \leqslant 0.
$$

This theory is now used here to develop high-order finite-difference schemes across interfaces where there is a step change in grid resolution, as shown diagrammatically in Fig. 1. By extension of the SBP property, finite-difference schemes that span the interface will also be stable, as long as the global structure of the H, P and Q matrices still follows these conditions. Note that the last point, 3, does not apply to the interface closure, only to the boundary.

3.1. Order of accuracy

In boundary and interface regions of the domain, the same accuracy conditions Eq. (7) apply, but to order $\sigma \leqslant s$. Because the global convergence rate of a finite-difference scheme can be made equal to that of the interior scheme if the boundary closure is one order less accurate [26], we typically use $\sigma = s - 1$. Therefore, to maintain fourth-order convergence, the boundaries must be third-order accurate, and in [19], a stable finite-difference approximation is developed at the boundaries that satisfies the order conditions to an accuracy one order less than that in the interior. Extending this result to the grid interface problem, the interior order of accuracy will still be preserved if the interface region is also one order less accurate than the interior scheme. However, because the result in [26] is an asymptotic convergence of the order of the interior stencil, it can be expected that the presence of many interface regions could degrade the convergence rate when compared to that of a uniform-grid because of the presence in the domain of several lower-order points; proportional to the number of interfaces.

3.2. Boundary condition

Essential to the stability of the finite-difference approximation is appropriate implementation of the boundary conditions, consistent with the SBP property and time stability. The Simultaneous Approximation Term (SAT) method described in [19] imposes the boundary condition using a penalty term, of strength τ, to enforce the condition $u(0, t) = g(t)$:

$$
P\frac{d\mathbf{u}}{dt} = -\frac{\lambda}{h}(Q\mathbf{u} - \tau\mathbf{S}(u_1 - g(t))), \tag{9}
$$

where

$$
\mathbf{S} = H^{-1}(w_{11}, 0, \ldots, 0)^{\mathrm{T}}. \tag{10}
$$

The eigenvalues of the matrix $-P^{-1}(Q - \tau[\mathbf{S0}\ldots\mathbf{0}])$ must have a negative real part for the overall scheme to be stable. In practice, this requires for the scalar advection equation that $\tau \geqslant 1$ [19].

4. Explicit interface closure

We consider first the interface problem with an explicit scheme of order $s = 4$ in the interior of the domain, where the derivative approximation is given by Eq. (5). The matrix P is the identity matrix in the interior region, while Q must be strictly antisymmetric locally. Furthermore, we observe that up to fourth-order accurate stencils, H can be taken equal to the identity matrix.

4.1. Scheme structure

Consider an n-points wide explicit interface closure with a five-point interior stencil in terms of parameters β and α. Then, in the region of the interface between grids of resolution h and rh, the local sections of the matrices P and Q have the form

$$P = \begin{bmatrix} D_p & A_p & 0 \\ A_p^{\mathrm{T}} & \widehat{P} & \widehat{A_p^{\mathrm{T}}} \\ 0 & \widehat{A_p^{\mathrm{TT}}} & rD_p \end{bmatrix}, \quad Q = \begin{bmatrix} D_q & A_q & 0 \\ -A_q^{\mathrm{T}} & \widehat{Q} & \widehat{A_q^{\mathrm{T}}} \\ 0 & -\widehat{A_q^{\mathrm{TT}}} & D_q \end{bmatrix}, \quad \text{with } A_q = \begin{bmatrix} 0 & 0 & 0 & \ldots \\ \alpha & 0 & 0 & \ldots \\ \beta & \alpha & 0 & \ldots \end{bmatrix}, \tag{11}$$

where $D_p = I$ is the identity matrix of size $k \times k$, D_q is the block-diagonal interior part of Q also of size $k \times k$, and $\widehat{P}$ and $\widehat{Q}$ represent the modified interface part of each matrix. For an interface closure of n-points, $\widehat{P}$ and $\widehat{Q}$ are square $n \times n$ matrices. The matrix A_q represents the overlapping part of Q over the interface stencil and is of size $k \times n$, and for the explicit case the corresponding part of P, $A_p = 0$. The superscript $\widehat{\mathrm{T}}$ denotes the flip-transpose, across the anti-diagonal, or in index notation by $a_{i,j}^{\mathrm{T}} = a_{n-j+1,k-i+1}$ for $A_q = \{a_{ij}\}$.

The accuracy conditions, Eq. (7), are applied at the interface in terms of the elements of $\widehat{P}$, $\widehat{Q}$ and A_q to order σ_i for interface nodes $i = -n/2, \ldots, n/2 - 1$ and for each $z = 0, \ldots, \sigma_i$. The order to which the accuracy condition is satisfied for node i, σ_i, is not necessarily the same for all nodes in the interface. The resulting system of equations generated by the accuracy conditions is reduced by the symmetry constraints of $\widehat{P}$ and the antisymmetric constraints of $\widehat{Q}$, but, depending on the size of the particular scheme, elements may remain unspecified by the accuracy conditions and lead to parametric families of closures. These parameters can be chosen to reduce the bandwidth of the stencil, and/or to modify the eigenvalues of $\widehat{P}$.

4.2. An explicit fourth-order interface closure

A fourth-order closure can be constructed by choosing $\alpha = -1/12$, $\beta = 2/3$ and $n = 4$, such that the matrices $\widehat{P}$ and $\widehat{Q}$ are given by

$$\widehat{P} = \begin{bmatrix} p_{11} & p_{12} & p_{13} & p_{14} \\ p_{12} & p_{22} & p_{23} & p_{24} \\ p_{13} & p_{23} & p_{33} & p_{34} \\ p_{14} & p_{24} & p_{34} & p_{44} \end{bmatrix}, \quad \widehat{Q} = \begin{bmatrix} 0 & q_{12} & q_{13} & q_{14} \\ -q_{12} & 0 & q_{23} & q_{24} \\ -q_{13} & -q_{23} & 0 & q_{34} \\ -q_{14} & -q_{24} & -q_{34} & 0 \end{bmatrix}. \tag{12}$$

Different closure schemes are identified here by the order of accuracy satisfied at each point in the interface region. We denote in compact form the order of accuracy of the interface closure by σ_{-2}–σ_{-1}–σ_0–σ_1 for $n = 4$. The ordering is assumed to be from left to right where the left side contains the fine grid. Thus, a 4–3–3–4 scheme has four points in the interface closure, the inner two of which satisfy the order conditions to third-order, and the outer two satisfy the conditions to fourth order. All interface closures considered here are symmetrically distributed about the grid interface, so a four-point scheme has two points in the coarse block and two in the fine block. The number of points used for a particular closure depends strongly on the size of the interior stencil. For a standard fourth-order interior scheme, a minimum of four points are required in the interface region, because the five-point stencil extends over both blocks for a distance of at least two points each side.

To maintain the global convergence rate s of the finite-difference scheme used in the interior of the domain, the order of accuracy at every point in the interface must be $\sigma \geqslant s - 1$. For a four-point scheme with

a fourth-order interior scheme, if each point in the interface is third order, there are a total of 16 equations in terms of the 16 independent coefficients of $\widehat{P}$ and $\widehat{Q}$. However, the set of equations is not linearly independent (this particular system has rank 14); they are insufficient to solve for all 16 variables uniquely. Therefore, to reduce the total truncation error of the scheme, two points can be solved up to fourth-order accuracy, giving 18 equations (in a system of rank 16) in the 16 coefficients, which has a unique solution for each particular arrangement of third- and fourth-order points across the interface. These solutions satisfy the SBP conditions on both $\widehat{P}$ and $\widehat{Q}$ and are stable for varying ranges of grid ratio, r. It is not possible for a third point in the four-point interface to be fourth-order; no more coefficients can be added to the matrices while still maintaining their SBP structure.

For the symmetric 4–3–3–4 interface scheme, applying Eq. (7) at the four interface nodes, yields the following four matrix equations:

$$
\begin{bmatrix} 0 & 0 & 0 & 0 \\ 1 & 1 & 1 & 1 \\ 0 & 2 & 3+r & 3+3r \\ 0 & 3 & \frac{3(3+r)^2}{4} & \frac{27(1+r)^2}{4} \\ 0 & 4 & \frac{(3+r)^2}{2} & \frac{27(1+r)^3}{2} \end{bmatrix}
\begin{bmatrix} p_{11} \\ p_{12} \\ p_{13} \\ p_{14} \end{bmatrix}
=
\begin{bmatrix} 1 & 1 & 1 \\ 1 & \frac{3+r}{2} & \frac{3+3r}{2} \\ 1 & \frac{(3+r)^2}{4} & \frac{9(1+r)^2}{4} \\ 1 & \frac{(3+r)^3}{8} & \frac{27(1+r)^3}{8} \\ 1 & \frac{(3+r)^4}{16} & \frac{81(1+r)^4}{16} \end{bmatrix}
\begin{bmatrix} q_{12} \\ q_{13} \\ q_{14} \end{bmatrix}
+
\begin{bmatrix} -\frac{7}{12} \\ \frac{1}{2} \\ -\frac{1}{3} \\ 0 \\ \frac{2}{3} \end{bmatrix},
\tag{13}
$$

$$
\begin{bmatrix} 0 & 0 & 0 & 0 \\ 1 & 1 & 1 & 1 \\ -2 & 0 & 1+r & 1+3r \\ 3 & 0 & \frac{3(1+r)^2}{4} & \frac{3(1+3r)^2}{4} \end{bmatrix}
\begin{bmatrix} p_{12} \\ p_{22} \\ p_{23} \\ p_{24} \end{bmatrix}
=
\begin{bmatrix} 1 & 1 & 1 \\ -1 & \frac{1+r}{2} & \frac{1+3r}{2} \\ 1 & \frac{(1+r)^2}{4} & \frac{(1+3r)^2}{4} \\ -1 & \frac{(1+r)^3}{8} & \frac{(1+3r)^3}{8} \end{bmatrix}
\begin{bmatrix} -q_{12} \\ q_{13} \\ q_{14} \end{bmatrix}
+
\begin{bmatrix} \frac{1}{12} \\ -\frac{1}{6} \\ \frac{1}{3} \\ -\frac{2}{3} \end{bmatrix},
\tag{14}
$$

$$
\begin{bmatrix} 0 & 0 & 0 & 0 \\ 1 & 1 & 1 & 1 \\ -3-r & -1-r & 0 & 2r \\ \frac{3(3+r)^2}{4} & \frac{3(1+r)^2}{4} & 0 & 3r^2 \end{bmatrix}
\begin{bmatrix} p_{13} \\ p_{23} \\ p_{33} \\ p_{34} \end{bmatrix}
=
\begin{bmatrix} 1 & 1 & 1 \\ -\frac{3+r}{2} & -\frac{1+r}{2} & r \\ \frac{(3+r)^2}{4} & \frac{(1+r)^2}{4} & r^2 \\ -\frac{(3+r)^3}{8} & -\frac{(1+r)^3}{8} & r^3 \end{bmatrix}
\begin{bmatrix} -q_{13} \\ -q_{23} \\ q_{34} \end{bmatrix}
-
\begin{bmatrix} \frac{1}{12} \\ \frac{r}{6} \\ \frac{r^2}{3} \\ \frac{2r^3}{3} \end{bmatrix},
\tag{15}
$$

$$
\begin{bmatrix} 0 & 0 & 0 & 0 \\ 1 & 1 & 1 & 1 \\ -3-3r & -1-3r & -2r & 0 \\ \frac{27(1+r)^2}{4} & \frac{3(1+3r)^2}{4} & 3r^2 & 0 \\ -\frac{27(1+r)^3}{2} & -\frac{(1+3r)^2}{2} & -4r^3 & 0 \end{bmatrix}
\begin{bmatrix} p_{14} \\ p_{24} \\ p_{34} \\ p_{44} \end{bmatrix}
=
-\begin{bmatrix} 1 & 1 & 1 \\ -\frac{3+3r}{2} & -\frac{1+3r}{2} & -r \\ \frac{9(1+r)^2}{4} & \frac{(1+3r)^2}{4} & r^2 \\ -\frac{27(1+r)^3}{8} & -\frac{(1+3r)^3}{8} & -r^3 \\ \frac{81(1+r)^4}{16} & \frac{(1+3r)^4}{16} & r^4 \end{bmatrix}
\begin{bmatrix} q_{14} \\ q_{24} \\ q_{34} \end{bmatrix}
+
\begin{bmatrix} \frac{7}{12} \\ \frac{r}{2} \\ \frac{r^2}{3} \\ 0 \\ -\frac{2r^4}{3} \end{bmatrix}.
\tag{16}
$$

Solving this system, the following expressions for the dependence on r of the elements of $\widehat{P}$ and $\widehat{Q}$ are obtained:

$$
p_{11} = \frac{1271r^6 - 418r^5 - 479r^4 + 28,676r^3 + 214,297r^2 + 467,870r + 279,503}{31,104(r+1)(r+3)^2},
$$

$$
p_{22} = \frac{1271r^6 + 11,934r^5 + 9761r^4 + 7812r^3 + 36,377r^2 + 12,510r + 1743}{3456(r+1)(3r+1)^2},
$$

$$
p_{33} = \frac{1743r^6 + 12,510r^5 + 36,377r^4 + 7812r^3 + 9761r^2 + 11,934r + 1271}{3456r^2(r+1)(r+3)^2},
$$

$$
p_{44} = \frac{279,503r^6 + 467,870r^5 + 214,297r^4 + 28,676r^3 - 479r^2 - 418r + 1271}{31,104r^2(r+1)(3r+1)^2},
$$

$$p_{12} = \frac{-1271r^6 - 5758r^5 + 1927r^4 + 5372r^3 + 11{,}095r^2 + 1154r + 1305}{10{,}368(3r^3 + 13r^2 + 13r + 3)},$$

$$p_{13} = -\frac{819r^6 + 7982r^5 + 4693r^4 + 4388r^3 + 1213r^2 - 16210r + 1723}{10{,}368r(r+1)(r+3)^2},$$

$$p_{14} = -\frac{-1723r^6 + 2642r^5 + 7099r^4 + 7004r^3 + 7099r^2 + 2642r - 1723}{31{,}104r(3r^3 + 13r^2 + 13r + 3)},$$

$$p_{23} = \frac{819r^6 - 2242r^5 + 1485r^4 + 25{,}988r^3 + 1485r^2 - 2242r + 819}{3456r(3r^3 + 13r^2 + 13r + 3)},$$

$$p_{24} = -\frac{1723r^6 - 16210r^5 + 1213r^4 + 4388r^3 + 4693r^2 + 7982r + 819}{10{,}368r(r+1)(3r+1)^2},$$

$$p_{34} = \frac{1305r^6 + 1154r^5 + 11{,}095r^4 + 5372r^3 + 1927r^2 - 5758r - 1271}{10{,}368r^2(3r^3 + 13r^2 + 13r + 3)},$$

$$q_{12} = \frac{545r^4 - 120r^3 + 2054r^2 + 1368r + 377}{216(3r^3 + 13r^2 + 13r + 3)}, \quad q_{13} = \frac{-193r^4 + 261r^3 - 181r^2 + 195r - 34}{216r(r^2 + 4r + 3)},$$

$$q_{14} = \frac{17r^4 - 63r^3 - 4r^2 - 63r + 17}{108r(3r^2 + 10r + 3)}, \quad q_{23} = \frac{193r^4 - 282r^3 + 754r^2 - 282r + 193}{72r(3r^2 + 10r + 3)},$$

$$q_{24} = \frac{-34r^4 + 195r^3 - 181r^2 + 261r - 193}{216r(3r^2 + 4r + 1)}, \quad q_{34} = \frac{377r^4 + 1368r^3 + 2054r^2 - 120r + 545}{216r(3r^3 + 13r^2 + 13r + 3)}. \tag{17}$$

These matrix elements as functions of r can then be used to impose the last condition, requiring that $\widehat{P}$ be positive definite. We have done this numerically and found that, for this 4–3–3–4 scheme, the range of values of r over which the minimum eigenvalue of $\widehat{P}$ is positive is $1/r_{\max} < r < r_{\max}$, where $r_{\max} \approx 4.551$.

If six points are used with a fourth-order interior scheme, there are now up to 36 independent coefficients of $\widehat{P}$ and $\widehat{Q}$ available, but no more than 30 equations (six rows, up to fourth-order accuracy in each). However, the maximum number of fourth-order points in a six-point interface scheme is five, because it is not possible algebraically to enforce the order conditions up to fourth-order at all points. Moreover, when comparing four- and six-point fourth-order interface schemes, it is important to note that although formal accuracy of the six-point scheme may be better (with a 4–4–3–4–4–4 scheme, or a truncation error-optimized 4–4–3–3–4–4), both are third-order at every point when implemented in an explicit finite-difference method. The formal accuracy at each point in the interface is correct for the original construction of Eq. (5), but when this is implemented by inverting P, every point in the block is reduced to third-order accuracy as the lower-order error is spread across the interface by the action of $\widehat{P}^{-1}$. This implies that, if the number of points in a block is relatively small compared to the number of interface points, then it is more desirable to minimize the width of the interface than to force fourth-order accuracy at a maximum number of points. For this reason, four-point interface closures for fourth-order interior schemes are presented here.

4.3. Inverse grid ratios

The grid ratio in the derivation thus far has been arbitrary. For $r > 1$, the solution corresponds to an interface between a fine grid and a coarse grid (moving from left to right), and for $r < 1$ it corresponds to the opposite case. A particular scheme may be solved for any grid ratio, up to the positive definite limit of $\widehat{P}$, and, for some closures, it is possible to derive the corresponding reflected stencil, that for $1/r$, directly from the stencil for r. Writing Eq. (5) for an interface $\frac{1}{r}{:}1$, in terms of the matrices $\widehat{P}$ and $\widehat{Q}$ of the $1{:}r$ interface, gives

$$\widehat{P}\frac{\mathrm{d}\mathbf{u}}{\mathrm{d}x} = \frac{r}{h}\widehat{Q}\mathbf{u},$$

or, alternatively,

$$\left(\frac{1}{r}\widehat{P}\right)\frac{\mathrm{d}\mathbf{u}}{\mathrm{d}x} = \frac{1}{h}\widehat{Q}\mathbf{u}. \tag{18}$$

The scheme for the inverse-ratio interface $1 : \frac{1}{r}$ may then be obtained, in the form of Eq. (5), by taking the transpose of the flip-transpose of the original matrices $\widehat{P}$ and $\widehat{Q}$ to give

$$\widehat{P}^* \frac{\mathrm{d}\mathbf{u}}{\mathrm{d}x} = \frac{1}{h}\widehat{Q}^* \mathbf{u}. \tag{19}$$

In terms of the elements $p_{i,j}$ of the original matrix, the elements of the transformed matrix $\widehat{P}^*$ are given by

$$p_{i,j}^* = \frac{1}{r}p_{n+1-i,n+1-j}, \tag{20}$$

and, similarly, the elements of $\widehat{Q}^*$ are given by

$$q_{i,j}^* = -q_{n+1-i,n+1-j}, \tag{21}$$

where n is the width of the interface. Note that the negative sign is necessary to preserve the antisymmetry of $\widehat{Q}^*$ after the transformation.

Generally, schemes with symmetric accuracy (like 4–3–3–4 or 4–4–3–3–4–4), are preferable to biased schemes (such as 3–3–4–4 or 4–4–4–3–4–4), as the symmetric schemes behave predictably for both transitions from a fine to a coarse grid, and from a coarse to a fine grid. If the accuracy conditions are applied symmetrically across the interface for a particular grid ratio r, then the stability of the inverse-ratio scheme for a grid ratio $1/r$ follows that of the parent scheme. If not, stability for a particular grid ratio does not imply stability of the inverse-ratio. For example, the fourth-order 4–3–3–4 scheme is stable for practical integer grid ratios in the range $\frac{1}{4} \leqslant r \leqslant 4$, but the biased 3–3–4–4 scheme, which is stable for $r = 8$, is unstable for $r = 1/8$. We suspect that this arises because, for $r > 1$, the third-order points are in the fine block, where the truncation error is $O(h^3)$, and the fourth-order points are in the coarse block, with an truncation error of $O((rh)^4)$. For large r and small h, the errors on both sides can be comparable in magnitude depending on $\mathbf{u}$. On the other hand, for a scheme with the third-order points in the coarse block (i.e. for $r < 1$), the truncation error there would be much larger than that in the fine block, adversely affecting stability. Unless a strongly directional refinement is necessary, symmetric interface closures are preferred in general.

5. Compact interface closure

For compact (Padé) finite-difference schemes, the first derivative approximation Eq. (5) leads to a matrix P that is typically tri- or penta-diagonal. This is advantageous computationally, as it can be solved efficiently using a fast algorithm [27]. In order to retain this computationally efficient structure and satisfy the SBP constraints in the interface closure, the matrix H now has a non-trivial form and the matrices $V = HP$ and $W = HQ$ are introduced. Note that while the accuracy conditions are applied to P and Q as before, the SBP structure is forced upon V and W instead.

5.1. Scheme structure

The matrices at the interface between grids of spacing h and rh have the form of Eq. (11) and

$$V = \begin{bmatrix} D_v & A_v & 0 \\ A_v^{\mathrm{T}} & \widehat{V} & rA_v^{\widehat{\mathrm{T}}} \\ 0 & rA_v^{\widehat{\mathrm{TT}}} & rD_v \end{bmatrix}, \quad W = \begin{bmatrix} D_w & A_w & 0 \\ -A_w^{\mathrm{T}} & \widehat{W} & A_w^{\widehat{\mathrm{T}}} \\ 0 & -A_w^{\widehat{\mathrm{TT}}} & D_w \end{bmatrix}, \tag{22}$$

with

$$A_v = \begin{bmatrix} 0 & 0 & 0 & \dots \\ a' & 0 & 0 & \dots \\ b' & a' & 0 & \dots \end{bmatrix} \quad \text{and} \quad A_w = \begin{bmatrix} 0 & 0 & 0 & \dots \\ \alpha' & 0 & 0 & \dots \\ \beta' & \alpha' & 0 & \dots \end{bmatrix}. \tag{23}$$

The matrix H has the structure

$$H = \begin{bmatrix} D_h & A_h & 0 \\ A_h^{\mathrm{T}} & \widehat{H} & A_h^{\widehat{\mathrm{T}}} \\ 0 & A_h^{\widehat{\mathrm{T}}\mathrm{T}} & D_h \end{bmatrix}, \quad \text{with } A_h = \begin{bmatrix} 0 & 0 & 0 & \dots \\ 0 & 0 & 0 & \dots \\ x & 0 & 0 & \dots \end{bmatrix}, \tag{24}$$

where D_v, D_w and D_h represent the block-diagonal interior part of each matrix, V, W and H, respectively. The interior part of H, D_h, is a Toeplitz tri-diagonal matrix of diagonal y and sub-diagonals x. The constants x and y are set by the boundary closure [19], and are considered known *a priori*. In order to recover P and Q, the matrices that are actually used by an implementation of the method, we multiply Eq. (11) by Eq. (24) and equate to Eq. (22). Introducing the generic A,

$$A = \begin{bmatrix} 0 & 0 & 0 & \dots \\ 0 & 0 & 0 & \dots \\ 1 & 0 & 0 & \dots \end{bmatrix}, \tag{25}$$

to express $A_p = aA$, $A_q = \beta A$, $A_h = xA$, etc., and applying the SBP constraints leads to the following relationships

$$\widehat{V} = \widehat{H}\widehat{P} + xa(A^{\mathrm{T}}A + rA^{\widehat{\mathrm{T}}}A^{\widehat{\mathrm{T}}\mathrm{T}}), \tag{26}$$

$$\widehat{W} = \widehat{H}\widehat{Q} + x\beta(A^{\mathrm{T}}A - A^{\widehat{\mathrm{T}}}A^{\widehat{\mathrm{T}}\mathrm{T}}), \tag{27}$$

$$0 = A\left(\widehat{P} - \frac{1}{r}\widehat{P^{\mathrm{T}}}\right), \tag{28}$$

$$0 = A(\widehat{H}^{\mathrm{T}} - \widehat{H^{\mathrm{T}}}), \tag{29}$$

$$0 = A(\widehat{Q} + \widehat{Q^{\mathrm{T}}}), \tag{30}$$

$$aA^{\mathrm{T}}D_h + x\widehat{P}^{\mathrm{T}}A^{\mathrm{T}} = xA^{\mathrm{T}}D_p + a\widehat{H}A^{\mathrm{T}}, \tag{31}$$

$$\beta D_h A + xA\widehat{Q} = -xD_q^{\mathrm{T}}A + \beta A\widehat{H}^{\mathrm{T}}. \tag{32}$$

The last five conditions reduce to four equations relating the elements of the first and last rows of $\widehat{P}$ and $\widehat{Q}$, and the first and last columns of $\widehat{H}$:

$$p_{1j} = \frac{1}{x}((xb - ya)\delta_{1j} + ah_{j1}), \quad j = 1, \dots, n, \tag{33}$$

$$p_{nj} = \frac{r}{x}((xb - ya)\delta_{nj} + ah_{jn}), \quad j = 1, \dots, n, \tag{34}$$

$$q_{1j} = -\frac{1}{x}(y\beta\delta_{1j} - \beta h_{j1}), \quad j = 1, \dots, n, \tag{35}$$

$$q_{nj} = \frac{1}{x}(y\beta\delta_{nj} - \beta h_{jn}), \quad j = 1, \dots, n, \tag{36}$$

where δ_{ij} is the Kronecker Delta. When combined with the accuracy conditions, these equations imply that for an interface region of n-points, the first and last rows of $\widehat{P}$ and $\widehat{Q}$, and the first and last columns of $\widehat{H}$, have the same values as the interior rows and columns, respectively, of each matrix. In this way, an n-point wide interface in $\widehat{V}$ and $\widehat{W}$ is reduced to a width of $n - 2$ points in $\widehat{P}$ and $\widehat{Q}$.

5.2. A compact fourth-order interface closure

The derivation of the compact scheme follows that of the explicit scheme, and in this case, the problem can be solved in the same manner, but in terms of $\widehat{V}$ and $\widehat{W}$. For a fourth-order compact closure, we need to consider a six-point wide interface stencil of the type 4–4–3–3–4–4, according to our notation. The symmetry and

antisymmetry of $\widehat{V}$ and $\widehat{W}$, respectively, is built into the structure of the matrices, and the constants take the values $x = -1/8$, $y = 1$, $\alpha' = -3/32$, $\beta' = 3/4$, $a' = -1/32$, $b' = 1/8$. An equivalent set of equations to (13)–(16) is obtained, now in terms of the elements of $\widehat{V}$ and $\widehat{W}$. Relating these to the elements of $\widehat{H}$, $\widehat{P}$ and $\widehat{Q}$ are an additional 72 equations that arise when the products in Eqs. (26) and (27) are expanded. The resulting quadratic system for the coefficients of $\widehat{V}$, $\widehat{W}$, $\widehat{H}$, $\widehat{P}$ and $\widehat{Q}$ appears to be over-determined, but is not and can be solved numerically to arbitrary precision. As noted, starting with a six-point stencil for $\widehat{V}$ and $\widehat{W}$, results in a four-point stencil for $\widehat{P}$ and $\widehat{Q}$. Moreover, we have imposed a tri-diagonal structure for $\widehat{P}$ to limit the computational cost of an implementation to that of the standard compact method. This gives matrices of the following forms:

$$\widehat{H} = \begin{bmatrix} y & h_{12} & h_{13} & h_{14} & h_{15} & 0 \\ x & y & h_{23} & h_{24} & h_{25} & 0 \\ 0 & h_{32} & y & h_{34} & h_{35} & 0 \\ 0 & h_{42} & h_{43} & y & h_{45} & 0 \\ 0 & h_{52} & h_{53} & h_{54} & y & x \\ 0 & h_{62} & h_{63} & h_{64} & h_{65} & y \end{bmatrix}, \tag{37}$$

$$\widehat{P} = \begin{bmatrix} b & a & 0 & 0 & 0 & 0 \\ p_{21} & p_{22} & p_{23} & 0 & 0 & 0 \\ 0 & p_{32} & p_{33} & p_{34} & 0 & 0 \\ 0 & 0 & p_{43} & p_{44} & p_{45} & 0 \\ 0 & 0 & 0 & p_{54} & p_{55} & p_{56} \\ 0 & 0 & 0 & 0 & ra & rb \end{bmatrix}, \quad \widehat{Q} = \begin{bmatrix} 0 & \beta & 0 & 0 & 0 & 0 \\ q_{21} & q_{22} & q_{23} & q_{24} & q_{25} & q_{26} \\ q_{31} & q_{32} & q_{33} & q_{34} & q_{35} & q_{36} \\ q_{41} & q_{42} & q_{43} & q_{44} & q_{45} & q_{46} \\ q_{51} & q_{52} & q_{53} & q_{54} & q_{55} & q_{56} \\ 0 & 0 & 0 & 0 & -\beta & 0 \end{bmatrix}. \tag{38}$$

We reproduce here the matrices $\widehat{H}$, $\widehat{P}$ and $\widehat{Q}$ (from which $\widehat{V}$ and $\widehat{W}$ can be obtained) for a grid ratio of $r = 2$ (Tables 1–3).

The scheme for the inverse-ratio $r = 1/2$ is developed from this one by the same procedure described for the explicit scheme. Fig. 2 shows the eigenvalue distributions of the matrix $-P^{-1}(Q - \tau \mathbf{S})$ for a domain of 24 points, having two blocks of 12 points each, with an interface between them of a grid ratio $r = 2$. The boundary closure used is that given in Appendix A for the compact fourth-order scheme. The $\tau \mathbf{S}$ term represents the

Table 1
Coefficients of $\widehat{H} = \{h_{ij}\}$ for $r = 2$

h_{12}	$-0.12324024847848997101643979162$
h_{13}	$-0.31333152752131113246166446 \times 10^{-1}$
h_{14}	$0.85269971985340694716421239894$ 3596×10^{-5}
h_{15}	$0.11860746785502789792431677280958178 \times 10^{-3}$
h_{23}	$0.61879049194364805969505025274 \times 10^{-1}$
h_{24}	$-0.30658237914330047503034463 6 \times 10^{-1}$
h_{25}	$0.40803323223721328264783822 \times 10^{-2}$
h_{32}	$-0.14028558242379875813142039 9$
h_{34}	$0.52392558002445079611153283 5 \times 10^{-1}$
h_{35}	$-0.12969386219201282257019202 3 \times 10^{-1}$
h_{42}	$0.10204306574998420540223697 3 \times 10^{-1}$
h_{43}	$-0.14702252987201355569786227 229 \times 10^{1}$
h_{45}	$-0.11575249667458256582304677 57$
h_{52}	$0.92012345275652849152437 36 \times 10^{-3}$
h_{53}	$-0.19896595626666399077096291 49$
h_{54}	$0.13595331494923112642912419 2$
h_{62}	$0.24615372487607313952940444 615678953 \times 10^{-3}$
h_{63}	$0.41175230765386509576000460 9 \times 10^{-1}$
h_{64}	$-0.30685956580377242369688257 2 \times 10^{-1}$
h_{65}	$-0.12543901701600804235995340 78$

Table 2
Coefficients of $\widehat{P} = \{p_{ij}\}$ for $r = 2$

p_{21}	$0.2424978853301560587789396958$
p_{22}	$0.106409044228026781720538998804 \times 10^1$
p_{23}	$-0.13262867616501410170117363483$
p_{32}	$0.4351123458346305481241106565 \times 10^{-1}$
p_{33}	$0.160802048028942154848725621265 \times 10^1$
p_{34}	$-0.78347874036222542470627430305 \times 10^{-1}$
p_{43}	$0.2369327790682670486055438309905 \times 10^1$
p_{44}	$0.1581194310546069842438403889705 \times 10^1$
p_{45}	$0.49607173110723153138130189045$
p_{54}	$0.51885613705189044164467563505 \times 10^{-1}$
p_{55}	$0.18455666682157422259993738106 \times 10^1$
p_{56}	$0.50327149569999915359504284435$

Table 3
Coefficients of $\widehat{Q} = \{q_{ij}\}$ for $r = 2$

q_{21}	$-0.76125776999234329947115965505$
q_{22}	$0.11432577940623282346047532025$
q_{23}	$0.84731715727001746654103511975$
q_{24}	$-0.23960132522322968364375430255$
q_{25}	$0.45258496632236574101638187405 \times 10^{-1}$
q_{26}	$-0.604233809291408871143246805 \times 10^{-2}$
q_{31}	$0.21663489405658970067492337 \times 10^{-2}$
q_{32}	$-0.81063929810578478468428100245$
q_{33}	$0.15446170548540313835421816725$
q_{34}	$0.77096613579953759971654605295$
q_{35}	$-0.12683997178558630092759069735$
q_{36}	$0.98850796658644744251896719 \times 10^{-2}$
q_{41}	$0.58847563645372666838194635 \times 10^{-2}$
q_{42}	$-0.97163625879009501953553619785$
q_{43}	$-0.62543594739052595845414433875$
q_{44}	$0.105174961440072888328020152165 \times 10^1$
q_{45}	$0.52890271505529722707641044225$
q_{46}	$0.10535120360057699305758147205 \times 10^{-1}$
q_{51}	$0.19529371529603868685573564 \times 10^{-2}$
q_{52}	$-0.49713104720348277795579079705 \times 10^{-1}$
q_{53}	$0.21798529104201816012948307405$
q_{54}	$-0.72732140303886238891074680225$
q_{55}	$-0.19093455708075995569429742095$
q_{56}	$0.74803083664499207653500519485$

application of the boundary condition for the advection equation by the SAT method, applied here at the upstream boundary in the first block. For this demonstration, a value $\tau = 2$ was used. We observe that the real part of each eigenvalue is indeed negative, so the scheme is guaranteed to be time stable.

6. Test examples

We describe four test cases, one linear and one nonlinear in both 1D and 2D. In all cases we use explicit third-order Runge–Kutta time integration with the maximum time step determined from a CFL-type condition of the form

$$\frac{u\Delta t}{h} \leqslant 1, \tag{39}$$

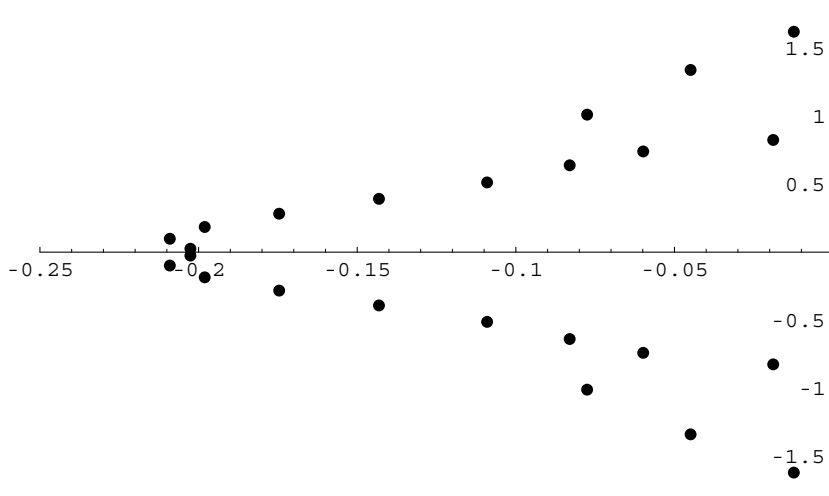where h denotes the smallest grid spacing and u is the appropriate convection speed.

Fig. 2. Eigenvalues of $-P^{-1}(Q - \tau \mathbf{S})$ for a 24-point domain, two blocks of 12 points each, first block with discretization h and the second with rh, for $r = 2$.

6.1. Advection equation

The boundary and interface schemes described here were tested with the linear advection equation, Eq. (1). Stability and convergence were tested by comparing the solution after multiple domain transition times with the analytic solution. Results are presented for the specific advection problem where

$$u(0, t) = -\sin \frac{2\pi \lambda t}{L}, \quad t \geqslant 0, \tag{40}$$

$$u(x, 0) = \sin \frac{2\pi x}{L}, \quad 0 \leqslant x \leqslant L, \tag{41}$$

with $\lambda > 0$, whose exact solution is

$$u(x, t) = \sin \frac{2\pi}{L}(x - \lambda t), \quad 0 \leqslant x \leqslant L, \ t \geqslant 0. \tag{42}$$

The boundary condition, Eq. (40), is applied by the SAT method, with $\tau = 2$, at the first node in the domain. As shown in Fig. 1, nodes are placed at the center of elements of width Δx, so the first node is at $\frac{\Delta x}{2}$, and the boundary condition is correspondingly adjusted. Under refinement, the width of each element (equivalent to the nodal spacing) is reduced and the number of nodes increased by the factor of refinement such that the physical location of the interfaces is fixed in space.

This problem is solved here using a fourth-order finite-difference scheme on a three-block grid, with 20 points in the first block and 10 in each of the subsequent blocks for the coarsest case. The first interface has $r = 4$ and the second $r = 1/2$. Five steps of global refinement are performed for the convergence test, from $h = 0.1$ to 0.0125. Solutions are presented for the case with $h = 0.05$, after two wave transitions through the domain $\left(T = 2\frac{L}{\lambda}\right)$. Fig. 3 shows a solution and the convergence results of the explicit scheme, using the four-point 4–3–3–4 interface closure described in Section 4 and the four-point 3–3–4–4 boundary closure given in Appendix A. The advertised fourth-order convergence rate clearly has been achieved, in both an averaged sense and uniformly, as evidenced by the slope of the L_∞ norm.

Fig. 4 shows a solution and the convergence study of the compact scheme, using the four-point interface closure derived in Section 5 with $r = 2$ and $r = 1/2$, and the four-point boundary closure given in Appendix A. This was tested on a three block 2:1:2 grid, with a minimum of 20 points in each block, the first interface having $r = 2$ and the second $r = 1/2$. Again, five steps of refinement were performed, over the same range of discretizations h, and the other solution parameters follow those used for the explicit test. The advertised fourth-order convergence rate clearly has again been achieved, in both an averaged sense and uniformly.
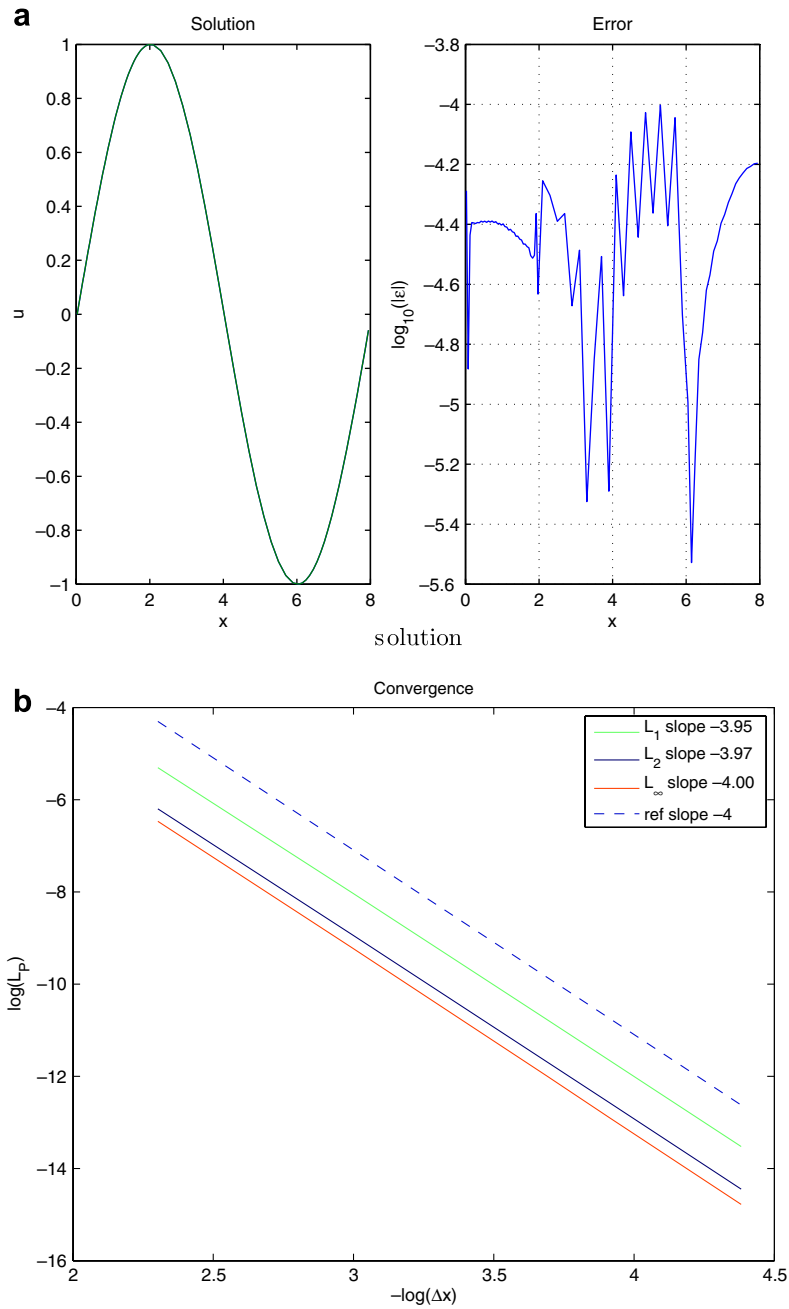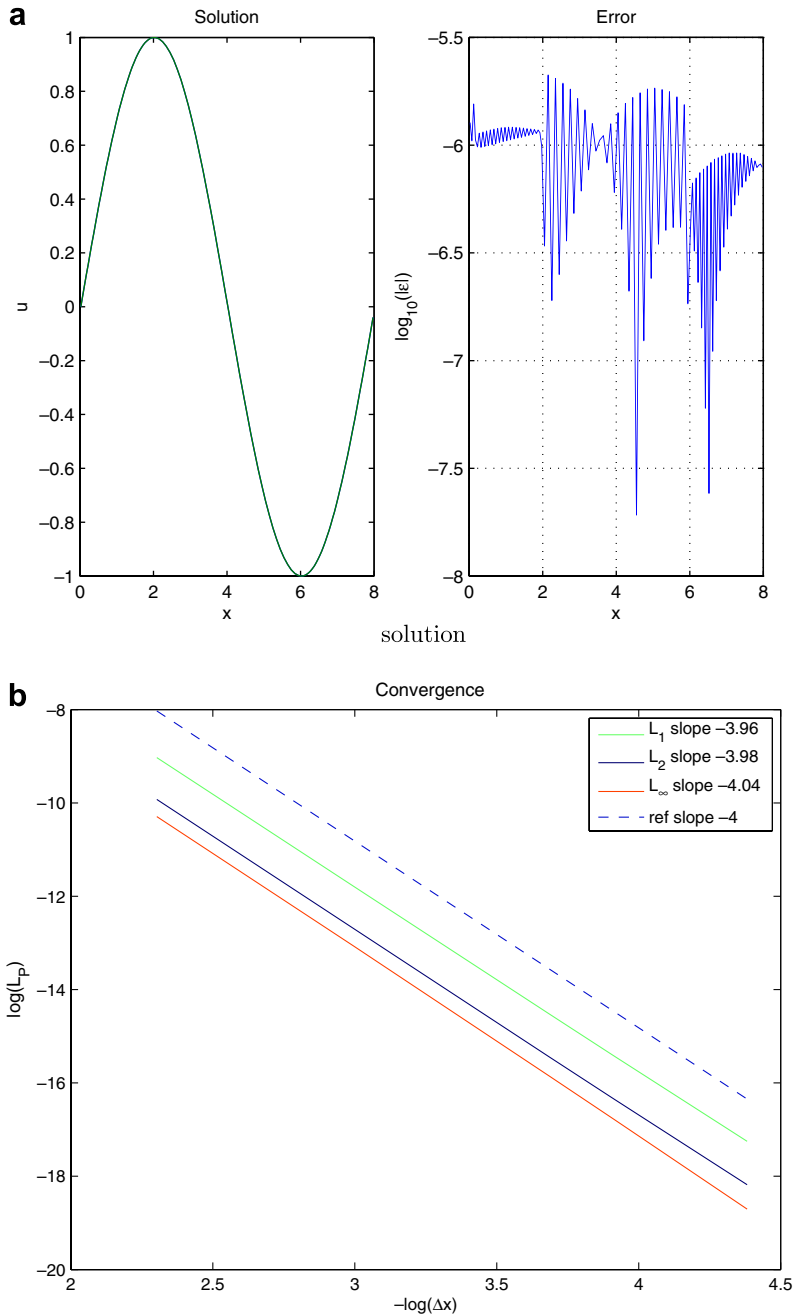
a

solution

b

Fig. 3. Advection equation solved with an explicit finite-difference scheme: (a) the numerical solution and error relative to the exact solution after two wave transitions for $h = 0.05$ and (b) a plot of the error convergence by L_1, L_2 and L_∞ norms. See text for description of the grid.

6.2. Navier–Stokes shock

To demonstrate the methods described here applied to a nonlinear problem, the one-dimensional compressible Navier–Stokes equations were solved for the flow through a shock. This problem can be solved analytically for the special case of constant viscosity with Prandtl number $Pr = 3/4$, so an accurate measure of error in the numerical solution can be made. In terms of dimensionless variables $\bar{\rho}$, $\bar{u}$ and $\bar{p}$ normalised by the

Fig. 4. Advection equation solved with a compact finite-difference scheme: (a) the numerical solution and error relative to the exact solution after two wave transitions for $h = 0.05$ and (b) a plot of the error convergence by L_1, L_2 and L_∞ norms. See text for description of the grid.

upstream flow states ρ_0, u_0 and p_0, and non-dimensional space $\xi = x/\lambda_0$ and time $\bar{t}$, the Navier–Stokes equations reduce to

$$\frac{\partial \bar{\rho}}{\partial \bar{t}} + \frac{\partial}{\partial \xi}(\bar{\rho}\bar{u}) = 0, \tag{43}$$

$$\frac{\partial}{\partial \bar{t}}(\bar{\rho}\bar{u}) + \frac{\partial}{\partial \xi}\left(\bar{\rho}\bar{u}^2 + \frac{1}{a_1}\bar{p} - a_3\frac{\partial \bar{u}}{\partial \xi}\right) = 0, \tag{44}$$

$$\frac{\partial}{\partial \bar{t}}(\bar{p} + a_1 a_2 \bar{\rho}\bar{u}^2) + \frac{\partial}{\partial \xi}\left(a_1 a_2 \bar{\rho}\bar{u}^3 + \gamma\bar{p}\bar{u} - 2a_1 a_2 a_3\bar{u}\frac{\partial \bar{u}}{\partial \xi} - \gamma a_3\frac{\partial}{\partial \xi}\left(\frac{\bar{p}}{\bar{\rho}}\right)\right) = 0, \tag{45}$$

with parameters $a_1 = \gamma M_0^2$, $a_2 = \frac{\gamma-1}{2}$ and $a_3 = \frac{4}{3}\frac{k}{\sqrt{\gamma M_0^2}}$, where $k = \frac{5}{8}\sqrt{\frac{\pi}{2}}$, derived from the kinetic theory constant $k_1 = \frac{5\pi}{32}$, γ is the ratio of specific heats, M_0 is the upstream Mach number and λ_0 is the upstream mean free path. This formulation reduces the number of problem parameters to γ and M_0.

For steady flow with $\partial/\partial\bar{t} \equiv 0$ in the frame of reference where the shock is stationary, and uniform upstream and downstream conditions such that $\bar{u} = 1$ upstream, the closed-form solution for the velocity profile through the shock is

$$\xi(\bar{u}) = \frac{1}{k_2(1-\alpha_1)M_0}\log\left[\left(\frac{\sqrt{\alpha_1}-\alpha_1}{\bar{u}-\alpha_1}\right)^{\alpha_1}\frac{\bar{u}-1}{\sqrt{\alpha_1}-1}\right], \tag{46}$$

where the velocity ratio $\alpha_1(M_0,\gamma)$ across the shock is given by the Rankine–Hugoniot relation

$$\alpha_1 = \frac{2 + (\gamma-1)M_0^2}{(\gamma+1)M_0^2}, \tag{47}$$

and the constant k_2 is given by

$$k_2 = \frac{3(\gamma+1)}{8k_1}\sqrt{\frac{\pi}{8\gamma}}. \tag{48}$$

In obtaining (46), $\xi = 0$ is chosen to correspond to the velocity inflection point, $\mathrm{d}^2\bar{u}/\mathrm{d}\xi^2 = 0$, which fixes the shock in space. For given γ and M_0, (46) can be solved numerically for $\bar{u}$ at each ξ to arbitrary precision; this gives the velocity profile through the shock, and subsequently the density and pressure profiles. We then proceed to solve (43)–(45) numerically as an initial-boundary-value problem using our interface schemes and consider convergence to Eq. (46).

As for the advection problem, a fourth-order finite-difference method is applied in the interior of the domain, with the four-point boundary and interface schemes described in this paper, for both explicit and compact stencils. Second derivatives are evaluated by applying the first derivative twice. The boundary conditions of the Navier–Stokes equations in compressible form must be carefully formulated, and are applied here in characteristic form, shown in Appendix B. Implementation is by the same SAT method described for the advection equation, with the parameter τ chosen appropriately for stability. Unlike the scalar advection equation or linear hyperbolic systems of equations, for this problem the stability bounds on τ are not as clear, but for a CFL number small enough, $\tau = 2$ was found to give stable solutions.

The shock problem was solved numerically on three representative domains: a uniform-grid, a three-block 1:4:1 grid with refinement in the vicinity of the shock, and a five-block 1:4:2:4:1 grid, with two levels of refinement near the shock, the interfaces of which are shown by the dashed lines in Fig. 5. The interfaces of the three-block grid have grid ratios $r_1 = 4$ and $r_2 = 1/4$, and the five-block grid has $r_1 = 4$, $r_2 = 2$, $r_3 = 1/2$ and $r_4 = 1/4$, moving from left to right across the domain. The numerical domain extended upstream of the shock to $\xi = -25$ and downstream to $\xi = 10$, at which point the difference between the analytic solution and the Rankine–Hugoniot conditions is of the order of machine precision (10^{-16}) for the chosen shock parameters. The initial condition used is the analytic solution, evaluated at the nodal positions. The discrete form of the Navier–Stokes equations is not identically satisfied by the continuous solution for finite h, so a third-order Runge–Kutta method is used to step the unsteady equations through time to obtain the steady numerical solution of the shock problem.

Results are presented here for a Mach 2.2 shock, with $\gamma = 1.4$. Convergence of the numerical solution error compared to the analytic solution, plotted against the minimum grid discretization h, shows the expected
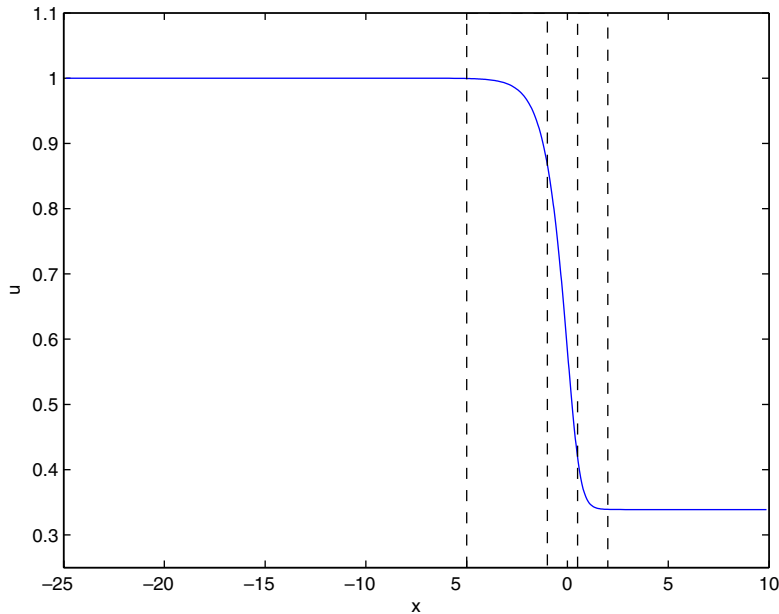
Fig. 5. Navier–Stokes shock solution, showing the locations of the interfaces in the five-block grid as dashed lines.

fourth-order slope in all three cases. Fig. 6 compares the convergence rates of the uniform-grid and three-block grid solutions, where the slope of the L_∞ norm indicates that the uniform-grid solution is uniformly fourth-order convergent, and the three-block grid solution approaches this limit. Here the asymptotic nature of the convergence described in [26] is apparent, as there are an increased number of third-order points in the three-block grid, introduced by the interface schemes, compared to the uniform-grid. This is also apparent in the similar convergence plot for the five-block grid.

Fig. 7 shows the numerical solutions for comparable uniform and three-block grids, with a plot of the error compared to the analytic solution Eq. (46). For the uniform-grid, the discretization of the solution shown is $h = 1/16$, for a total of 560 points in the domain, while for the three-block grid, the solution shown has the same discretization of $h = 1/16$ in the refined region of the shock, and 1/4 elsewhere, for a total of 200 points. With the same time step size, the computational cost of the three-block grid is approximately half that of the uniform-grid. Fig. 8 shows the behavior of the error in the time derivative terms of the equations of motion, in the form of the L_2 norm of the time derivative at each time step, for each of the continuity, momentum and energy equations, and a total norm of the three equation norms. Some oscillatory behavior is observed in the solution during the transient phase, but for long times the solution appears to be converging to a stable state.

The shock problem was also solved on a three-block 1:2:1 grid using the compact finite-difference scheme described in Section 5. Results from this test are shown in Fig. 9, showing (a), the solution at the final time step for a 400-point grid with smallest discretization $h = 1/20$, and (b), that near-fourth-order convergence is achieved.

6.3. 2D advection equation

Although the interface closure is developed here in a one-dimensional sense, it may be applied to certain two-dimensional grids, if the refinement is designed in such a way that it may be represented as a tensor product of 1D grids. A two-dimensional patch-refined grid in the sense of AMR, with cell-centered nodes, cannot be solved with this closure, because under refinement in both directions, nodes are no longer aligned across the interfaces, resulting in hanging nodes so derivatives in both directions must be considered simultaneously when building an interface scheme. This is the subject of ongoing research. Fig. 10 shows the type of locally-refined grid that can be solved with the current scheme.
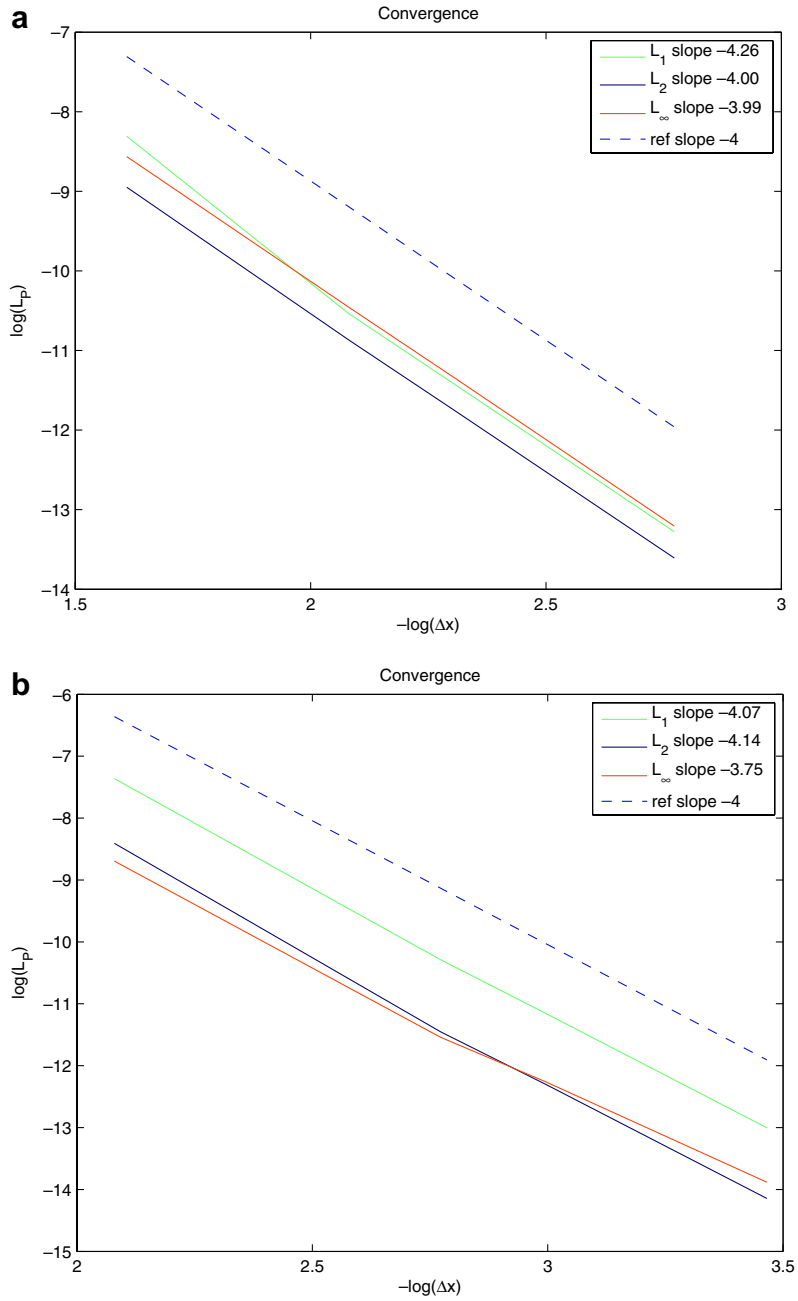
Fig. 6. Navier–Stokes shock solution convergence by each norm.

The two-dimensional scalar advection equation,

$$\frac{\partial u}{\partial t} + \lambda_1 \frac{\partial u}{\partial x} + \lambda_2 \frac{\partial u}{\partial y} = 0, \quad 0 \leqslant x \leqslant 1, \ 0 \leqslant y \leqslant 1, \ t \geqslant 0, \tag{49}$$

$$u(0, y, t) = \sin[\omega(y/\lambda_2 - 2t)], \tag{50}$$

$$u(x, 0, t) = \sin[\omega(x/\lambda_1 - 2t)], \tag{51}$$
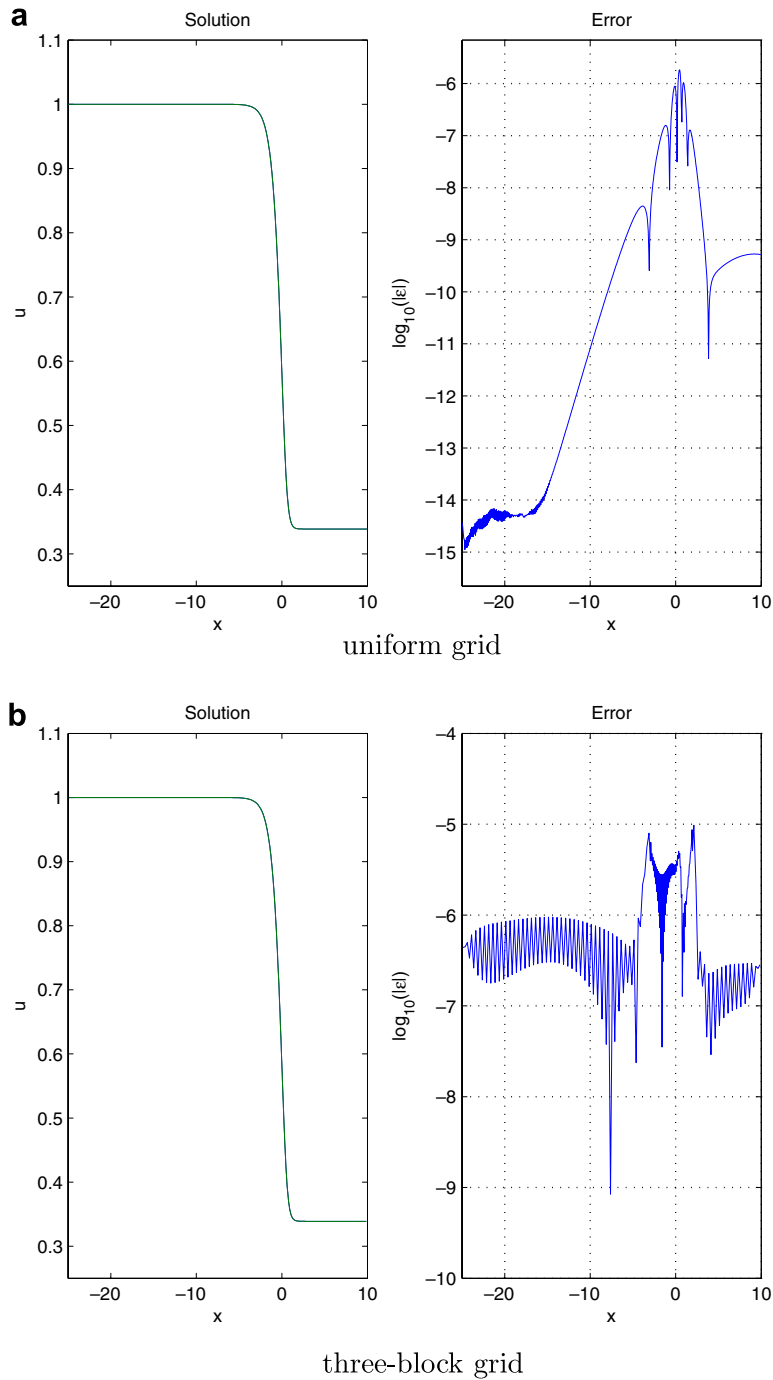
$$u(x, y, 0) = \sin[\omega(x/\lambda_1 + y/\lambda_2)], \tag{52}$$

Fig. 7. Numerical Navier–Stokes shock velocity solution, normalized by the upstream velocity, and the corresponding point-wise error. Both uniform and three-block grids shown here have the same minimum discretization, $h = 1/16$, for a total of 560 points and 200 points, respectively.

where λ_1 and λ_2 represent the advection speeds in the x- and y-directions, respectively, and ω is a frequency parameter, has analytic solution

$$u(x, y, t) = \sin[\omega(x/\lambda_1 + y/\lambda_2 - 2t)], \tag{53}$$
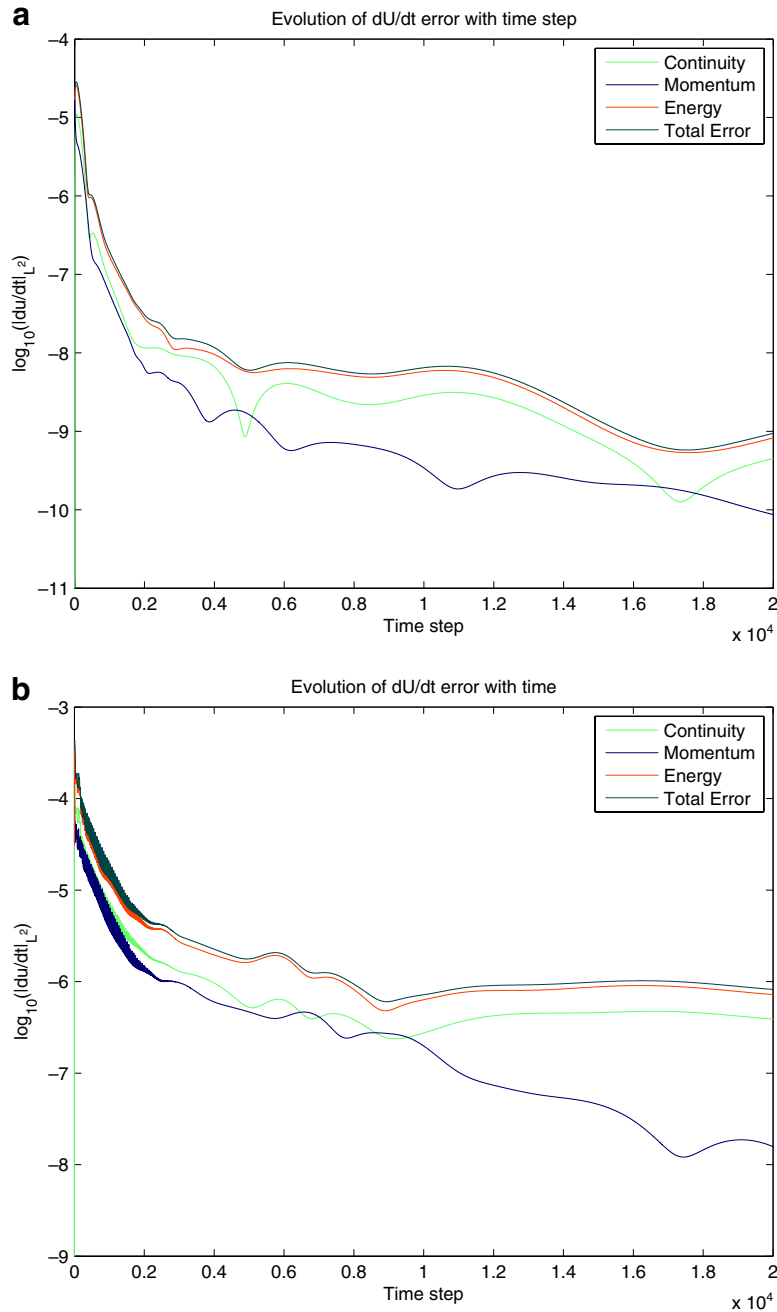
Fig. 8. Behavior of the time derivatives of the equations of motion for the numerical solution for the grids shown in Fig. 7.

and is solved here by a similar implementation as used for the 1D advection equation. The grid used is a unit square with each direction identically divided into five blocks, for a total of 25 blocks, with a factor of two refinement between each block for an overall 4:2:1:2:4 scheme ($r = 2$ for the first two interfaces, $r = 1/2$ for the next two). In each direction, the first and last blocks have a minimum of 10 points each, and each of the three remaining blocks has 8 points. Three steps of global refinement were performed for the convergence tests, from $h = 1/120$ to $1/360$. The same discretization was used in both x- and y-directions.
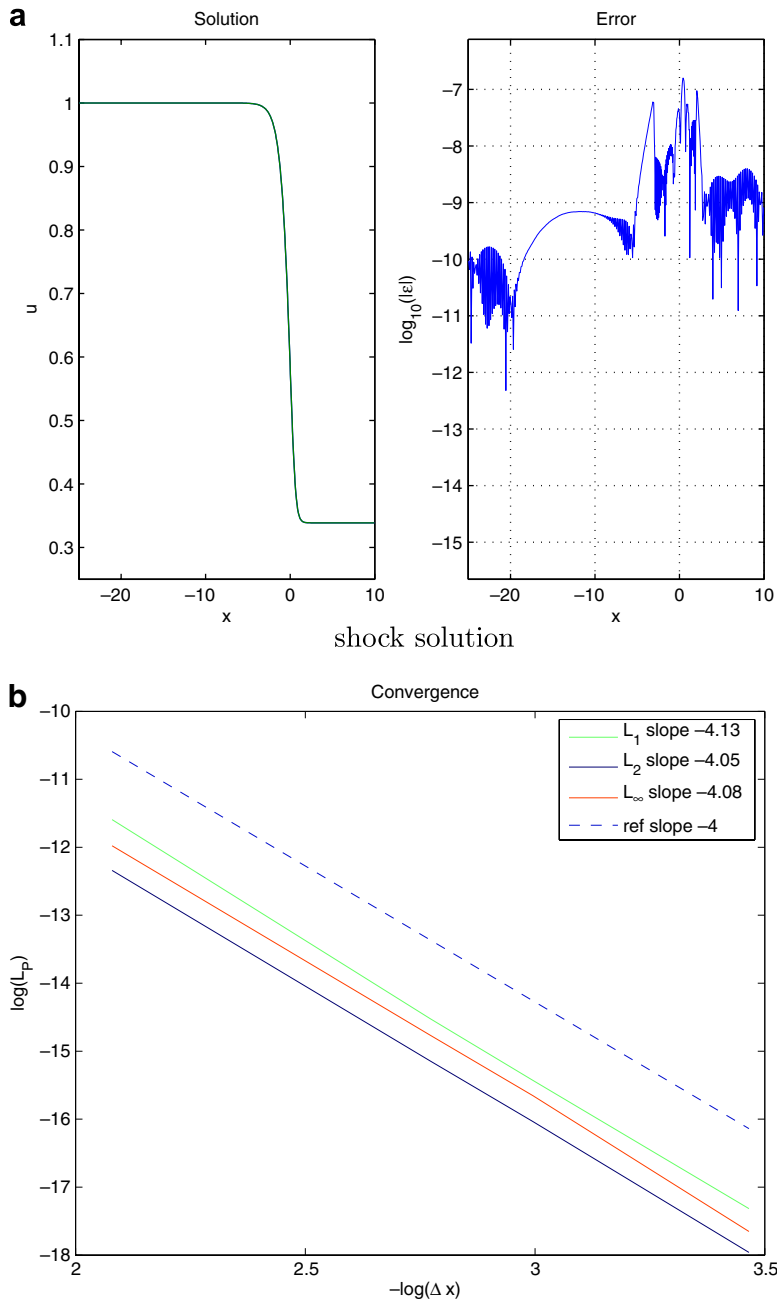
Fig. 9. Navier–Stokes shock velocity solution using compact finite-difference scheme: (a) solution at the final time step on a three-block 1:2:1 grid with minimum discretization $h = 1/20$ and (b) convergence plot.

Both fourth-order explicit and compact schemes were tested on this grid. Boundary conditions were implemented by the SAT method, using the same boundary closures as before. The test problem uses parameter values $\lambda_1 = \lambda_2 = 1/4$ and $\omega = \pi/2$, and was run to time $T = 10$. Fig. 11 shows that both average and uniform fourth-order convergence is achieved, for both explicit and compact schemes.
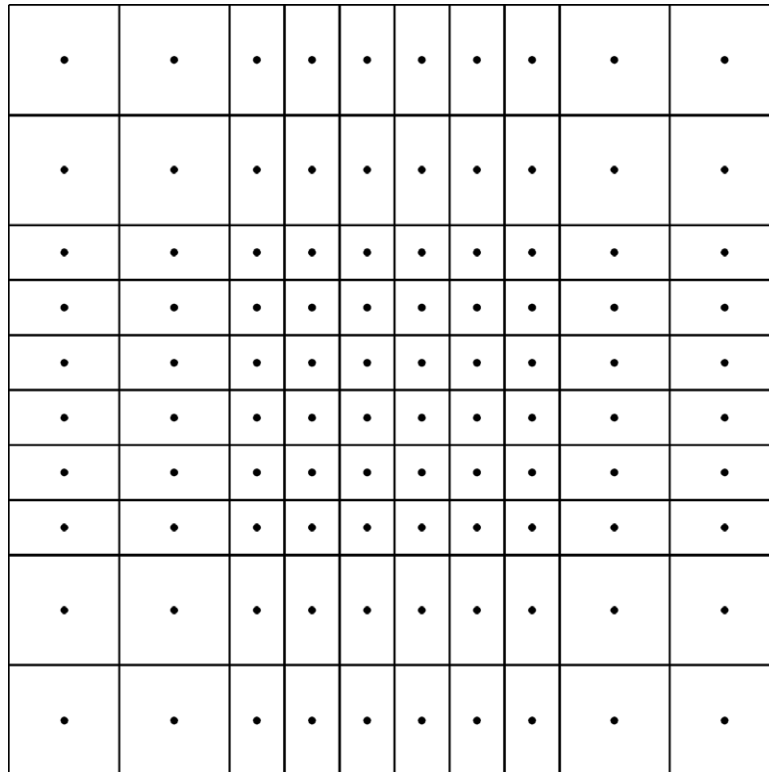
Fig. 10. An example of the type of local refinement on a two-dimensional grid that may be solved using the interface closure scheme presented here. This grid has one level of refinement in each direction.

6.4. 2D inviscid compressible vortex

For the final example, a nonlinear problem is solved on a similar locally-refined two-dimensional grid. Here, the dimensionless compressible Euler equations,

$$\frac{\partial \rho}{\partial t} + \frac{\partial}{\partial x}(\rho u) + \frac{\partial}{\partial y}(\rho v) = 0, \tag{54}$$

$$\frac{\partial}{\partial t}(\rho u) + \frac{\partial}{\partial x}\left(\rho u^2 + \frac{p}{\gamma M_0^2}\right) + \frac{\partial}{\partial y}(\rho uv) = 0, \tag{55}$$

$$\frac{\partial}{\partial t}(\rho v) + \frac{\partial}{\partial x}(\rho uv) + \frac{\partial}{\partial y}\left(\rho v^2 + \frac{p}{\gamma M_0^2}\right) = 0, \tag{56}$$

$$\frac{\partial}{\partial t}\left(\frac{p}{\gamma M_0^2} + \frac{\gamma-1}{2}\rho(u^2+v^2)\right) + \frac{\partial}{\partial x}\left(\frac{pu}{M_0^2} + \frac{\gamma-1}{2}\rho u(u^2+v^2)\right) + \frac{\partial}{\partial y}\left(\frac{pv}{M_0^2} + \frac{\gamma-1}{2}\rho v(u^2+v^2)\right) = 0, \tag{57}$$

are used with a normalization in terms of far-field values, ρ_0 and p_0, and a velocity scale, u_0, which are incorporated into the Mach number, M_0. An analytic solution exists for a constant-entropy vortex with the tangential velocity profile

$$\frac{u_\theta}{u_0} = \frac{r_0}{r}\left(1 - e^{-\frac{r^2}{r_0^2}}\right), \tag{58}$$
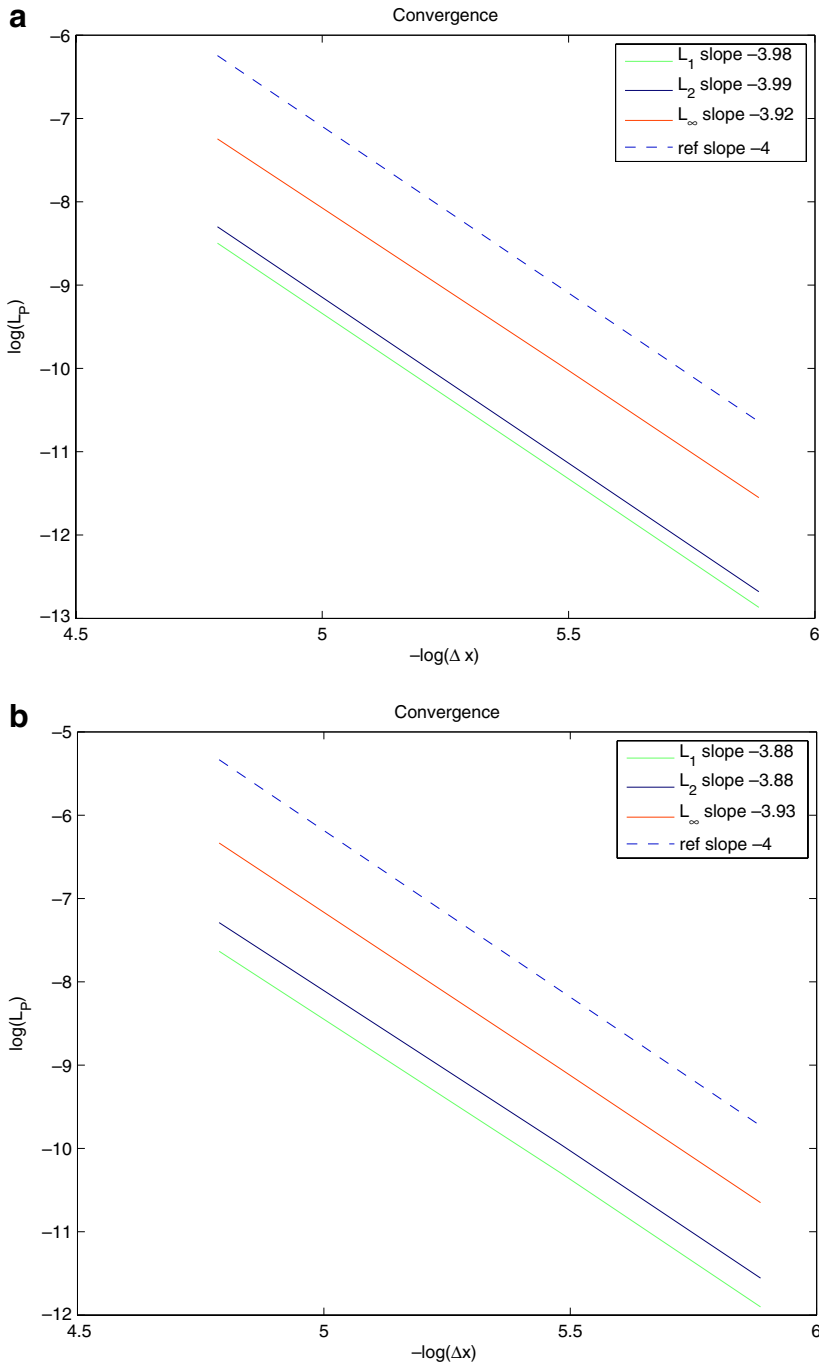
Fig. 11. Convergence plots for the 2D advection equation, using both explicit and compact schemes, showing that fourth-order convergence has been achieved.

where $r = \sqrt{x^2 + y^2}$ and r_0 is the core radius of the vortex. The corresponding pressure distribution is given by

$$\frac{p}{p_0} = \left(1 - (\gamma - 1)M_0^2 \left[\frac{r_0^2}{2r^2} \left(1 - \mathrm{e}^{-\frac{r^2}{r_0^2}} \right)^2 + \mathrm{Ei}\left(-2\frac{r^2}{r_0^2}\right) - \mathrm{Ei}\left(-\frac{r^2}{r_0^2}\right) \right] \right)^{\frac{\gamma}{\gamma-1}}, \tag{59}$$

where Ei(z) is the exponential integral function and the density is related to pressure by $p/p_0 = (\rho/\rho_0)^\gamma$. Analysis shows that, for $\gamma = 1.4$, as long as M_0 is less than approximately 1.35, the flow is subsonic everywhere (based on local Mach number), and for $M_0 < 1.9$, there is no evacuation at the core of the vortex. Parameter values of $M_0 = 1.2$ and $r_0 = 4/25$ were chosen for our test.

The discretized problem is solved on a grid similar to that used for the advection problem of Section 6.3, in a domain of side length 4. The same 4:2:1:2:4 refinement in each direction is used, now with a minimum of 14 points in the coarse blocks, 16 in the intermediate blocks and 24 in the most refined central block for an 84×84-node grid at the largest minimum discretization ($h = 1/50$). Five steps of global refinement were
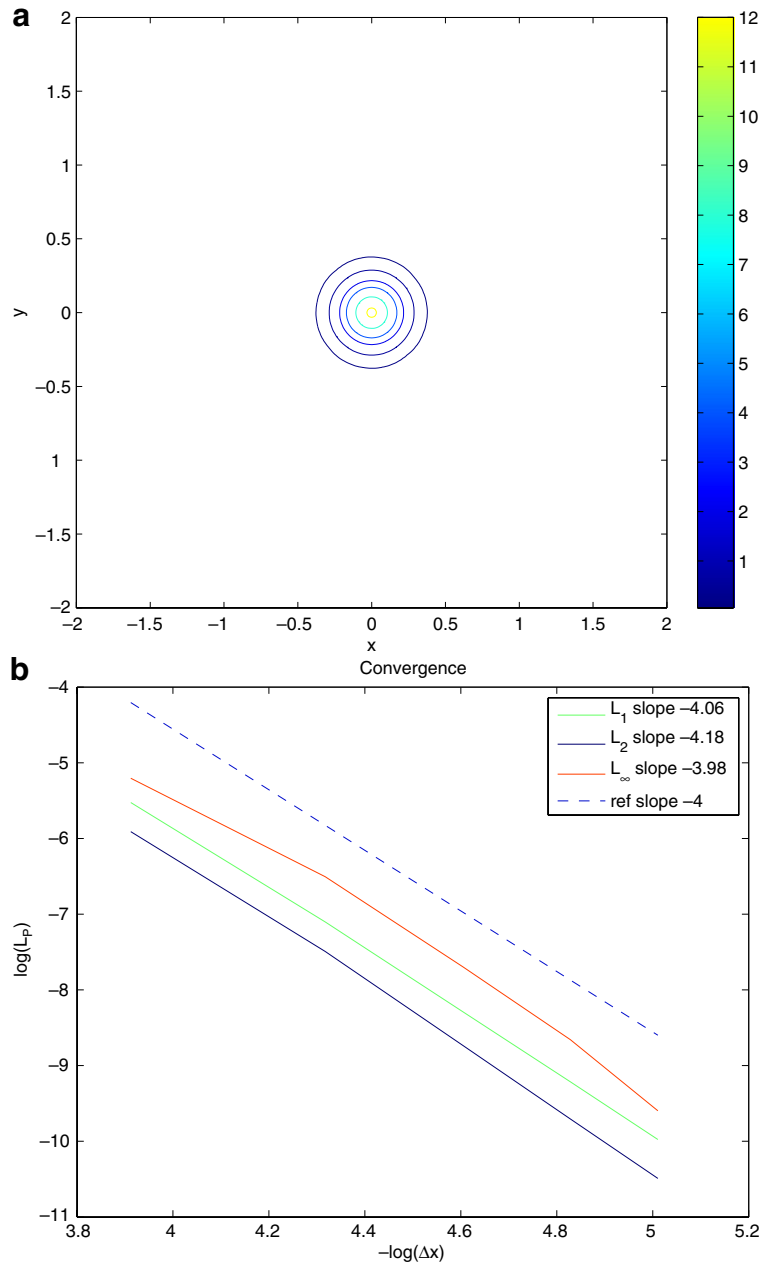

Fig. 12. Compressible vortex solution for a static centered vortex: (a) contours of vorticity for $h = 1/100$ and (b) convergence plot showing that fourth-order convergence is achieved.
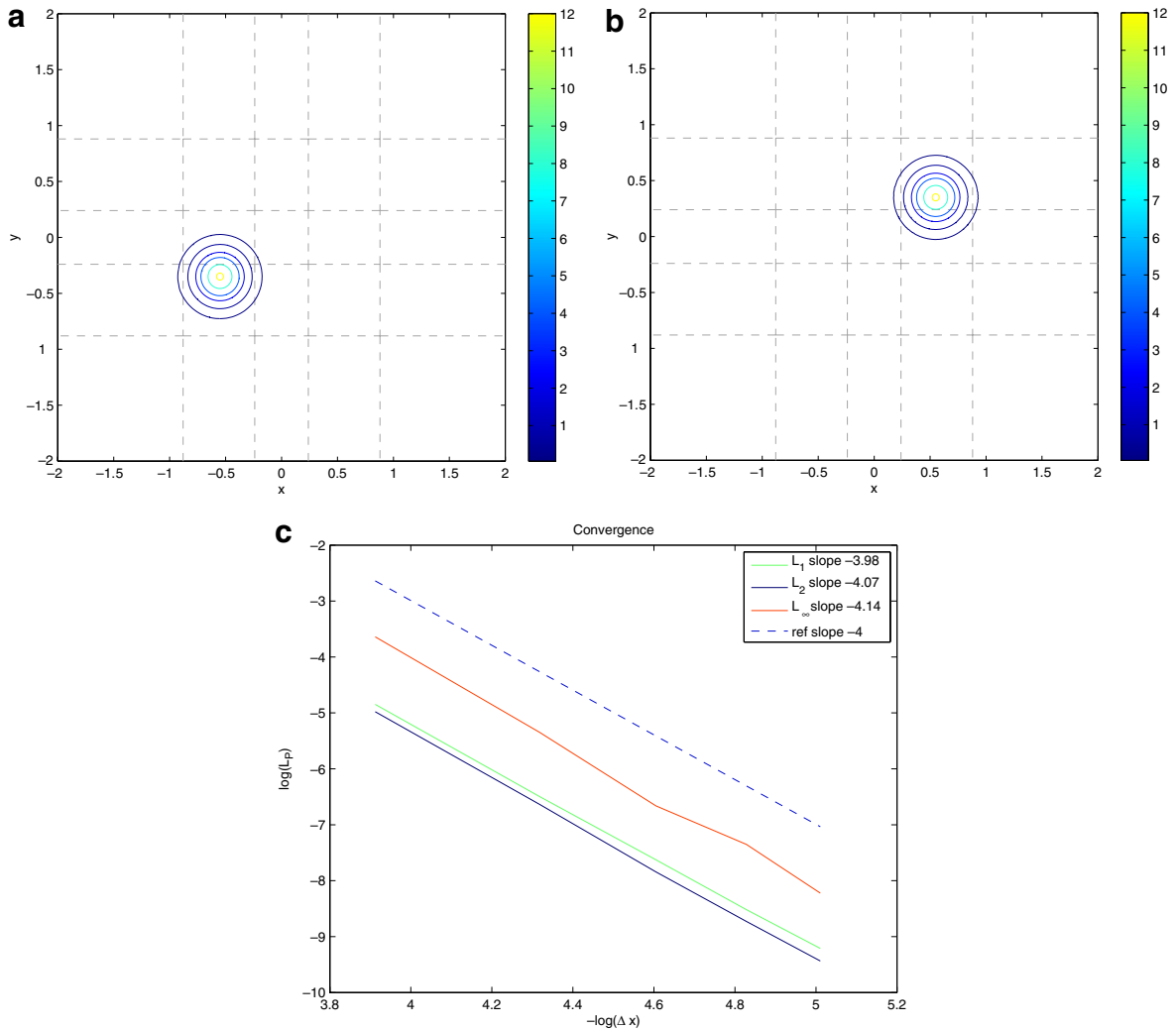
Fig. 13. Compressible vortex solution for a vortex convecting across the domain: plots (a) and (b) show for $h = 1/150$ contours of vorticity with the grid interfaces marked with dashed lines, at the beginning and end of the simulation, respectively, and plot (c) shows that fourth-order convergence is again achieved.

performed for the convergence test, down to $h = 1/150$ and a 252×252-node grid. Exact boundary conditions are applied on all edges, using the analytic solution (58) and (59), with the explicit finite-difference scheme. Results are given at time $t = 2$ for both a static vortex located at the center of the domain (Fig. 12), and for a vortex convecting across the domain with speed $(0.35, 0.55)$. The initial condition for the convecting vortex is such that at $t = 1$, the core is centered in the domain, and it thus moves from one side of the most refined region to the other during the simulation. This is shown in the vorticity contour plots of Fig. 13, where the grid interfaces are indicated by dashed lines. Convergence plots, shown in Figs. 12(b) and 13(c), demonstrate that fourth-order convergence is obtained for both examples.

7. Conclusions

We present an extension of the stable boundary closure theory for high-order finite-difference approximations to the case of step resolution changes at grid interfaces, which appear in adaptive mesh refinement. The closures are energy stable and satisfy the summation-by-parts condition by construction, while main-

taining the global order of accuracy of the interior scheme and avoiding numerical dissipation. This has been achieved for both explicit and compact interior schemes, to fourth-order and for large grid ratios in one dimension.

Numerical tests of these schemes using the scalar advection equation confirms that the global order of accuracy, s, of the interior finite-difference approximation is maintained when the interface scheme is of order $\sigma \geqslant s - 1$. This is shown in one dimension, and for the two-dimensional case on an appropriately refined grid. Applications of this method to the one-dimensional compressible Navier–Stokes equations to solve the shock structure problem, and to the two-dimensional compressible Euler equations to solve the vortex problem, show that the method is applicable to nonlinear systems of equations, giving stable results with the expected convergence rate as the spatial discretization is refined.

Acknowledgments

Appendix A. Stable boundary schemes

A.1. Explicit fourth-order boundary closure

The boundary closure derivation follows the theory of [18], but was applied here in a form analogous to that used for the interface schemes. Four points are sufficient to close the boundary problem to third-order at the outer two points and fourth-order at the inner two points, without free parameters. The scheme is described here as 3–3–4–4, following the naming convention given to the interface schemes, where the numbers refer to the order of accuracy at each point, and the domain end being at the left-hand side. Given here are the first six rows and columns of the P and Q matrices of this boundary scheme:

$$P = \begin{bmatrix} \frac{2429}{10,368} & \frac{469}{3456} & -\frac{113}{1152} & \frac{277}{10,368} & 0 & 0 \\ \frac{469}{3456} & \frac{4871}{3456} & -\frac{721}{3456} & \frac{205}{3456} & 0 & 0 \\ -\frac{113}{1152} & -\frac{721}{3456} & \frac{3623}{3456} & -\frac{43}{3456} & 0 & 0 \\ \frac{277}{10,368} & \frac{205}{3456} & -\frac{43}{3456} & \frac{10,397}{10,368} & 0 & 0 \\ 0 & 0 & 0 & 0 & 1 & 0 \\ 0 & 0 & 0 & 0 & 0 & 1 \end{bmatrix}, \tag{A.1}$$

$$Q = \begin{bmatrix} -\frac{1}{2} & \frac{167}{216} & -\frac{149}{432} & \frac{31}{432} & 0 & 0 \\ -\frac{167}{216} & 0 & \frac{133}{144} & -\frac{65}{432} & 0 & 0 \\ \frac{149}{432} & -\frac{133}{144} & 0 & \frac{143}{216} & -\frac{1}{12} & 0 \\ -\frac{31}{432} & \frac{65}{432} & -\frac{143}{216} & 0 & \frac{2}{3} & -\frac{1}{12} \\ 0 & 0 & \frac{1}{12} & -\frac{2}{3} & 0 & \frac{2}{3} \\ 0 & 0 & 0 & \frac{1}{12} & -\frac{2}{3} & 0 \end{bmatrix}. \tag{A.2}$$

The right-hand boundary is obtained from the left by the transpose/flip-transpose transformation. The summation-by-parts constraints are met by the boundary closure when combined with the SAT method for application of the boundary conditions.

A.2. Compact fourth-order boundary closure

The four-point compact boundary closure used in this work is that developed in [19], and is presented here for completeness. This scheme has third-order accuracy at each of the four points of the boundary region, and has P tri-diagonal to preserve the efficient structure of the interior scheme. Reproduced below are the four rows and columns of the boundary part of the H, P and Q matrices from [19]:

$$
H = \begin{bmatrix}
\frac{70{,}282{,}007{,}653}{7{,}658{,}388{,}480} & -\frac{9{,}426{,}299}{2{,}268{,}480} & -\frac{192{,}913}{1{,}067{,}520} & 0 \\[4pt]
-\frac{55{,}530{,}689{,}643}{2{,}552{,}796{,}160} & \frac{8{,}051{,}589}{756{,}160} & \frac{149{,}823}{355{,}840} & 0 \\[4pt]
\frac{63{,}842{,}626{,}133}{2{,}552{,}796{,}160} & -\frac{9{,}153{,}739}{756{,}160} & -\frac{4433}{355{,}840} & -\frac{1}{8} \\[4pt]
-\frac{71{,}498{,}870{,}443}{7{,}658{,}388{,}480} & \frac{10{,}110{,}149}{2{,}268{,}480} & \frac{102{,}703}{1{,}067{,}520} & 1
\end{bmatrix},
\tag{A.3}
$$

$$
P = \begin{bmatrix}
\frac{211}{429} & 1 & 0 & 0 \\[4pt]
1 & \frac{3563}{1688} & -\frac{1}{8} & 0 \\[4pt]
0 & \frac{43}{17} & \frac{1893}{1054} & \frac{139}{186} \\[4pt]
0 & 0 & \frac{1}{4} & 1
\end{bmatrix}, \quad
Q = \begin{bmatrix}
-\frac{289}{234} & \frac{279}{286} & \frac{75}{286} & -\frac{7}{2574} \\[4pt]
-\frac{8635}{3376} & \frac{6987}{3376} & \frac{1851}{3376} & -\frac{203}{3376} \\[4pt]
-\frac{15{,}043}{18{,}972} & -\frac{4089}{2108} & \frac{147}{124} & \frac{29{,}353}{18{,}972} \\[4pt]
0 & 0 & -\frac{3}{4} & 0
\end{bmatrix}.
\tag{A.4}
$$

As for the explicit scheme, the right-hand boundary scheme is obtained by transformation of the above left-hand side matrices.

Appendix B. Boundary conditions for the Navier–Stokes shock

Following from the dimensionless formulation of the Navier–Stokes Eqs. (43)–(45), the conserved vector of state U is given by

$$
U = [\bar{\rho}, \bar{\rho}\bar{u}, \bar{p} + a_1 a_2 \bar{\rho}\bar{u}^2]^{\mathrm{T}},
\tag{B.1}
$$

and the characteristic variable vector W, from the corresponding Euler (inviscid) form of the equations, is given by

$$
W = \left[\bar{u} - \frac{2}{\gamma - 1} c^*, \frac{\bar{p}}{\bar{\rho}^\gamma}, \bar{u} + \frac{2}{\gamma - 1} c^* \right]^{\mathrm{T}},
\tag{B.2}
$$

where c^* is the modified sound speed given by $c^* = \frac{1}{M_0} \sqrt{\frac{\bar{p}}{\bar{\rho}}}$. The components of W correspond to the characteristics $\lambda_1 = \bar{u} - c^*$, $\lambda_2 = \bar{u}$ and $\lambda_3 = \bar{u} + c^*$.

For a supersonic inlet and subsonic outlet, all the characteristics upstream of the shock must be specified, along with the incoming characteristic downstream. The final boundary condition, to close the problem, is to specify a zero temperature gradient at the downstream end. The resulting system of equations to be solved, with the terms due to the application of the boundary conditions by the SAT method included, is then given in terms of the conserved vector of state U by

$$
\frac{\partial U_1}{\partial \bar{t}} = -\frac{\partial F_1(U)}{\partial \xi} - \frac{\bar{\rho}}{2c^*}(\bar{u} - c^*)B_1 - \frac{1}{a_1}\frac{\bar{\rho}^\gamma \bar{u}}{c^{*2}}B_2 + \frac{\bar{\rho}}{2c^*}(\bar{u} + c^*)B_3,
\tag{B.3}
$$

$$
\frac{\partial U_2}{\partial \bar{t}} = -\frac{\partial F_2(U)}{\partial \xi} - \frac{\bar{\rho}}{2c^*}(\bar{u} - c^*)^2 B_1 - \frac{1}{a_1}\frac{\bar{\rho}^\gamma \bar{u}^2}{c^{*2}}B_2 + \frac{\bar{\rho}}{2c^*}(\bar{u} + c^*)^2 B_3,
\tag{B.4}
$$

$$
\frac{\partial U_3}{\partial \bar{t}} = -\frac{\partial F_3(U)}{\partial \xi} - a_1 a_2 \frac{\bar{\rho}}{2c^*}(\bar{u} - c^*)\left(\bar{u}^2 - 2\bar{u}c^* + \frac{c^{*2}}{a_2} \right)B_1 - a_2 \frac{\bar{\rho}^\gamma \bar{u}^3}{c^{*2}}B_2 + a_1 a_2 \frac{\bar{\rho}}{2c^*}(\bar{u}
$$
$$
+ c^*)\left(\bar{u}^2 + 2\bar{u}c^* + \frac{c^{*2}}{a_2} \right)B_3,
\tag{B.5}
$$

where the SAT penalty terms have the form

$$
B_1 = \tau \mathbf{S}_L[w_1^1 - g_1(\bar{t})], -\tau \mathbf{S}_R[w_1^N - h_1(\bar{t})],
$$
$$
B_2 = \tau \mathbf{S}_L[w_2^1 - g_2(\bar{t})],
$$
$$
B_3 = \tau \mathbf{S}_L[w_3^1 - g_3(\bar{t})],
$$

the parameters a_1 and a_2 are defined as before, $F(U)$ is the vector of fluxes, and $g(\bar{t})$ is the vector of boundary data at the upstream end and $h(\bar{t})$ is the boundary data at the downstream end.

References

[1] L. Jameson, AMR vs. high order methods, J. Sci. Comp. 18 (1) (2003) 1–24.

[2] M.J. Berger, J. Oliger, Adaptive mesh refinement for hyperbolic partial-differential equations, J. Comput. Phys. 53 (3) (1984) 484–512.

[3] M.J. Berger, P. Colella, Local adaptive mesh refinement for shock hydrodynamics, J. Comput. Phys. 82 (1) (1989) 64–84.

[4] M. Berger, Stability of interfaces with mesh refinement, Math. Comput. 45 (172) (1985) 301–318.

[5] M. Gerritsen, P. Olsson, Designing and efficient solution strategy for fluid flows. II: Stable high-order central finite difference schemes on composite adaptive grids with sharp shock resolution, J. Comput. Phys. 147 (2) (1998) 293–317.

[6] K. Sebastian, C-W. Shu, Multidomain WENO finite difference method with interpolation at subdomain interfaces, J. Sci. Comp. 19 (1) (2003) 405–438.

[7] P. Lötstedt, S. Söderberg, A. Ramage, L. Hemmingsson-Fråndén, Implicit solution of hyperbolic equations with space-time adaptivity, BIT 42 (1) (2002) 134–158.

[8] L. Ferm, P. Lötstedt, Accurate and stable grid interfaces for finite volume methods, Appl. Numer. Math. 49 (2004) 207–224.

[9] D-I. Choi, J.D. Brown, B. Imbiriba, J. Centrella, P. MacNeice, Interface conditions for wave propagation through mesh refinement boundaries, J. Comput. Phys. 193 (2) (2004) 398–425.

[10] B. Gustafsson, H.-O. Kreiss, A. Sundström, Stability theory of difference approximations for mixed initial boundary value problems II, Math. Comput. (1972).

[11] M. Ciment, Stable difference schemes with uneven mesh spacings, Math. Comput. 25 (114) (1971) 219–227.

[12] M. Ciment, Stable matching of difference schemes, SIAM J. Numer. Anal. 9 (4) (1972) 695–701.

[13] L.N. Trefethen, Stability of finite-difference models containing two boundaries or interfaces, Math. Comput. 45 (172) (1985) 279–300.

[14] F. Collino, T. Fouquet, P. Joly, A conservative space-time mesh refinement method for the 1D wave equation. Part II: Analysis, Numer. Math. 95 (2003) 223–251.

[15] G. Browning, H.-O. Kreiss, J. Oliger, Mesh refinement, Math. Comput. 27 (121) (1973) 29–39.

[16] R. Vichnevetsky, Wave propagation and reflection in irregular grids for hyperbolic equations, Appl. Numer. Math. 3 (1987) 133–166.

[17] B. Cathers, S. Bates, Spurious numerical refraction, Int. J. Numer. Meth. Fluid 21 (1995) 1049–1066.

[18] B. Strand, Summation by parts for finite difference approximations for d/dx, J. Comput. Phys. 110 (1) (1994) 47–67.

[19] M.H. Carpenter, D. Gottlieb, S. Abarbanel, Time-stable boundary conditions for finite difference schemes solving hyperbolic systems: methodology and application to high-order compact schemes, J. Comput. Phys. 111 (2) (1994) 220.

[20] S.S. Abarbanel, A.E. Chertock, Strict stability of high-order compact implicit finite-difference schemes: the role of boundary conditions for hyperbolic PDE's, I, J. Comput. Phys. 160 (2000) 42–66.

[21] J. Nordström, M.H. Carpenter, Boundary and interface conditions for high-order finite-difference methods applied to the Euler and Navier–Stokes equations, J. Comput. Phys. 148 (1999) 621–645.

[22] J. Nordström, R. Gustafsson, High order finite difference approximations of electromagnetic wave propagation close to material discontinuities, J. Sci. Comp. 18 (2) (2003) 215–234.

[23] P. McCorquodale, P. Colella, D.P. Grote, J.-L. Vay, A node-centered local refinement algorithm for poisson's equation in complex geometries, J. Comput. Phys. 201 (2004) 34–60.

[24] S.K. Lele, Compact finite difference schemes with spectral-like resolution, J. Comput. Phys. 103 (1992) 16–42.

[25] G. Scherer, On energy estimates for difference approximations to hyperbolic partial differential equations, Ph.D. Thesis, Department of Scientific Computing, Uppsala University, 1977.

[26] B. Gustafsson, The convergence rate for difference approximations to mixed initial boundary value problems, Math. Comput. 29 (130) (1975) 396–406.

[27] W.F. Ames, Numerical Methods for Partial Differential Equations, second ed., Academic Press, 1977.